

Bars and Warps traced by the Molecular Gas in the Seyfert 2 Galaxy NGC 1068

E. Schinnerer ¹, A. Eckart, L.J. Tacconi, R. Genzel
Max-Planck-Institut für extraterrestrische Physik, 85740 Garching, Germany

and

D. Downes
Institut de Radio Astronomie Millimétrique, 38406 Saint Martin d'Hères, France

Received _____; accepted _____

¹Present address at: California Institute of Technology, Pasadena, CA 91125

²Ap.J. accepted

ABSTRACT

We present new interferometer observations of the ^{12}CO (1–0) and ^{12}CO (2–1) line emission of NGC 1068 with a resolution of $0.7''$. The molecular gas in the inner $5''$ is resolved into a ring with two bright knots east and west of the nuclear continuum emission. For the first time in NGC 1068, we can trace molecular gas at $\approx 0.18''$ (13 pc) from the nucleus. The high velocities in this region imply an enclosed mass of $\sim 10^8 M_\odot$. This value is consistent with a black hole mass of $1.7 \times 10^7 M_\odot$, as estimated from nuclear H_2O maser emission, plus a contribution from a compact nuclear stellar cluster. Perpendicular to the kinematic major axis optical images of NGC 1068 show a bright, stellar, oval structure of eccentricity 0.8 and a deprojected length of 17 kpc. Analysis of the rotation curve shows the CO spiral arms are at the inner Lindblad resonance of this bar-like structure. Inside the molecular spiral arms, $10''$ from the nucleus, the CO kinematic axis changes direction probably in response to the to the 2.5 kpc (deprojected) long stellar bar seen in the near infrared (NIR). The low velocity dispersion indicates the molecular gas is in a disk with a thickness of 10 pc in the nuclear region and 100 pc in the spiral arms.

We constructed kinematic models for the molecular gas using elliptical orbits caused by a $\sim 1''$ (72 pc) nuclear bar and using tilted rings resulting in a warp. We find that the gas motions are consistent with either the warp or the bar models. However, because there is no evidence for a $\sim 1''$ nuclear bar in NIR images, we favor the warp model. A warped CO disk can also explain the obscuration of the AGN, the extinction of light from the nuclear stellar cluster, and the observed NIR and mid-IR polarization. The model predicts the warped CO disk should become edge-on at a radius of 70 pc, thereby creating a cavity for the ionization cone.

Subject headings: galaxies: ISM - galaxies: nuclei of - radio lines: ISM - galaxies: individual (NGC 1068)

1. INTRODUCTION

Knowledge of the distribution and kinematics of the circumnuclear molecular gas in Seyfert galaxies is essential for understanding the fueling of the central region and the role of gas and dust in obscuring the active galactic nucleus (AGN). Recent improvements in millimeter interferometry now allow us to observe molecular lines with sub-arcsecond resolution, high spectral resolution, and high sensitivity. In nearby Seyfert galaxies, with the best resolution currently available, we can now search for molecular gas down to radii of a few tens of parsecs. Models of the motions of this molecular gas can then help us to understand the mechanism that transports gas into the center.

An overview of the modeling results so far is given in Schinnerer, Eckart & Tacconi (1999a; hereafter SET99a), and a detailed model of the nuclear molecular gas in the Seyfert 1 galaxy NGC 3227 is given by Schinnerer, Eckart & Tacconi (1999b; hereafter SET99b). In the inner 80 pc of NGC 3227, for example, the kinematics of the molecular gas are better explained by a warping of the thin gas disk than by motion in the potential of a nuclear stellar bar. In that galaxy, molecular gas is detected down to a radius of ~ 10 pc.

In this paper, we model the complex kinematics of the central few hundred parsecs of the Seyfert 2 galaxy NGC 1068. This galaxy is at a distance of 14.4 Mpc ($H_0 = 75 \text{ km s}^{-1}$; see Bland-Hawthorn et al. 1997), giving a scale of 72 pc arcsec $^{-1}$ (**Table 1**), which is very favorable for detailed studies of the circumnuclear gas. NGC 1068 was originally classed as a Seyfert 2 galaxy based on its direct-path, i.e. unpolarized emission lines, which have narrow widths (Khachikian & Weedman 1974). This narrow-line region (NLR) is extended to the northeast of the nucleus and coincides with the radio jet. Antonucci & Miller (1985) later showed that the scattered-path, polarized emission lines have widths typical of broad-line regions (BLR), indicating that NGC 1068 has a hidden Seyfert 1 nucleus. Around this nucleus, there is a central nuclear star cluster with a FWHM diameter of 0.6'' (43 pc) that was mapped by Thatte et al. (1997). On a much larger scale, there is a stellar bar 2.3 kpc long, detected in the NIR (Scoville et al. 1988; Thronson et al. 1989). This bar is in turn surrounded by a circumnuclear starburst ring that, along with other star forming regions, contributes half the bolometric luminosity of the galaxy (Telesco et al. 1984; Davies et al. 1998). This starburst ring is also detected in lines of molecular gas (Planesas et al. 1991; Jackson et al. 1993; Tacconi et al. 1994; Helfer & Blitz 1995; Tacconi et al. 1997) and in the radio continuum (e.g. Gallimore et al. 1996).

The plan of this paper is as follows. Section 2 describes the observations and data reduction. Section 3 covers the distribution and kinematics of the CO emission, the millimeter continuum, and the location of the nucleus. In section 4 we derive the rotation curve of the molecular gas and discuss its relation to the stellar bar and the location of dynamical resonances. We then derive the molecular gas mass and the total dynamical mass (section 5) and derive the thickness of the molecular gas disk from the velocity dispersion (section 6). In section 7, we fit the kinematic data with bar and warp models. and discuss the model results in section 8. Section 9 summarizes our conclusions.

2. OBSERVATIONS AND DATA REDUCTION

The ^{12}CO lines were observed in February/March 1997 with the IRAM interferometer on Plateau de Bure, France, with 5 antennas in the long-baseline A, B1, and B2 configurations and in November 1995 to March 1996 with 4 antennas in the shorter-baseline C1, C2, and D1 configurations. The ^{12}CO (1–0) observations had baselines from 24 to 408 m that gave a beam of $2.2'' \times 1.2''$ at p.a. 26° after uniform weighting. The ^{12}CO (2–1) observations had only the A, B1, and B2 baselines, ranging from 40 to 408 m, that gave a beam of $1.0'' \times 0.5''$ (p.a. 26°) after uniform weighting. The bandpass was calibrated on 3C454.3 and 3C345. The source 0235+164 was observed every 10 min for phase and amplitude calibration. The data were CLEANed with 700 iterations and convolved to beams of $1.4'' \times 1.4''$ at ^{12}CO (1–0) and $0.7'' \times 0.7''$ at ^{12}CO (2–1), with velocity channels of 10 km s^{-1} for both lines. We also made a 115 GHz continuum map from the line-free channels from -310 to -190 km s^{-1} and $+200$ to $+320 \text{ km s}^{-1}$. To estimate the line flux, we subtracted the mean continuum from the channels with (line+continuum).

Our ^{12}CO (1–0) map agrees well with CO maps made with other interferometers, and our integrated ^{12}CO (1–0) flux agrees with that in the interferometer spectrum of Helfer & Blitz (1995) to within 15%. Helfer & Blitz (1995) also combined their BIMA array and NRAO single dish data. Their BIMA/NRAO map has 25 to 30% more flux than their BIMA map alone, so some of the large-scale flux may be resolved out by the BIMA and IRAM arrays. To check our calibration of the ^{12}CO (2–1) line emission, we made a ^{12}CO (2–1) map with the same beam as our ^{12}CO (1–0) map. At a resolution of $1.4''$, the $\frac{\text{CO}(2-1)}{\text{CO}(1-0)}$ ratio for the nuclear ring is $1.0 (\pm 20\%)$, in agreement with the ratio of 1.1 found in this region with the IRAM 30 m telescope (Braine & Combes 1992).

3. MOLECULAR GAS DISTRIBUTION AND PROPERTIES

3.1. The distribution of the line emission

Our new observations allow us to study the millimeter molecular line and continuum emission at an unprecedented angular resolution. The ^{12}CO (2–1) data, in particular, give very detailed maps of the molecular gas in the inner 200 pc of NGC 1068. At 100 pc from the center, the ^{12}CO (2–1) emission is in a ring (hereafter the *nuclear ring*; **Fig. 1**). In this nuclear ring, there are two emission knots, one at $1''$ east of the nucleus and another one $1.5''$ west and $1''$ south of the center. At $\pm 0.5''$ north and south of the center, there are emission ridges connecting the two knots at 25% of the peak line intensity. This same overall nuclear structure also exists in the CS(2–1) line (Tacconi et al. 1997) and the HCN(1–0) line (Tacconi et al. 1994). The $\frac{\text{CO}(2-1)}{\text{CO}(1-0)}$ ratio is between 0.8 and 1.0 over the entire nuclear ring, except for a part of the western emission knot, which has a ratio of 2.0. This is also evident in the nuclear spectra. The ^{12}CO (2–1) profile has three peaks while the ^{12}CO (1–0) profile has only two. The missing peak in the ^{12}CO (1–0) line is offset by

$+75\text{ km s}^{-1}$ relative to the systemic velocity and is associated with the western knot. This suggests the CO lines are optically thin in parts of the western knot.

As shown in earlier maps, most of the ^{12}CO (1–0) emission is in two spiral arms with a diameter of $\sim 40''$ (**Fig. 1**; Planesas et al. 1991; Kaneko et al. 1992; Helfer & Blitz 1995). On our new map, the ^{12}CO (1–0) peak $\sim 1''$ east of the center is 1.5 times stronger than the spiral-arm emission. In our map, the northern spiral arm is less luminous than the southern one, in contrast to the earlier measurements of Helfer & Blitz (1995; see below).

CO emission is also observed along the NIR stellar bar found by Scoville et al. (1988) at about half of the nuclear peak intensity. With our $1.4''$ beam, we mainly find emission in the northern half of the bar. In the lower resolution ($\sim 3.4''$) ^{12}CO (1–0) data (Tacconi et al. 1997) emission is seen on both sides of the bar, but stronger north of the nucleus. Both sides of the bar were also detected in lower resolution ^{12}CO (1–0) maps by Helfer & Blitz (1995) and in the ^{13}CO (1–0) map by Tacconi et al. (1997). The tips of the NIR stellar bar almost touch the spiral arms. The spiral arms are not detected in the ^{12}CO (2–1) map, because their diameter is larger than the $22''$ primary beam of the IRAM antennas, and a mosaic map would be needed to recover the spiral arms in ^{12}CO (2–1) . Furthermore, the spiral arms are weaker than the nucleus and they may be partly resolved since we only used long baseline configurations for the ^{12}CO (2–1) mapping.

Our ^{12}CO (1–0) intensity map agrees well with the OVRO map (Baker & Scoville 1998; private communication). Differences with the earlier data of Helfer & Blitz (1995) may be due to uncertainties in the calibration and deconvolution of the BIMA/NRAO data and the possibility that 30% of the extended line flux is resolved out in our interferometer map.

3.2. Radio continuum emission

Our 115 GHz continuum map shows two emission knots, one coinciding with the nucleus, and the other $2.5''$ east and $4.5''$ north of the nucleus (**Fig. 2**). The nuclear knot is slightly resolved by our $1.4''$ beam. A Gaussian fit gives $1.5'' \times 1.7''$ at p.a. 156° . At 115 GHz, the nuclear knot has a flux density of (36 ± 5) mJy, while the northern knot has (15 ± 5) mJy. The northern knot coincides with the peak of the 5 GHz radio jet mapped by Wilson & Ulvestad (1983), as noted previously by Helfer & Blitz (1995), who observed the same two continuum knots in their BIMA map at 85 GHz. This structure at 85 GHz is also observed with the IRAM array (Tacconi 1999; private communication). At 85 GHz, both knots have the same flux density, 40 mJy. At 230 GHz, no continuum emission was detected, to a limit of 6 mJy at each knot.

4. GLOBAL KINEMATICS OF THE MOLECULAR GAS

In this section, we describe the velocity field of the molecular gas, estimate the enclosed nuclear mass, and derive a rotation curve. We then combine this rotation curve with optical and IR evidence for bars in NGC 1068 to deduce the locations of dynamical resonances.

4.1. The large-scale CO velocity field

A striking feature of the ^{12}CO (1–0) velocity field is the change of position angle of the kinematic major axis within the spiral arms (**Fig. 3 a and c**). At radii $> 15''$ the velocity field of the molecular gas joins the outer HI velocity field at p.a. 280° and inclination 40° (Brinks et al. 1997). At $r < 10''$, the kinematic major axis changes its position angle from 278° to 305° . The change in position angle at $r \sim 10''$ also occurs in the velocity fields of the $\text{H}\alpha$ (Dehnen et al. 1997) and the stars (Garcia-Lorenzo et al. 1997). This effect also appears in the $\text{HCN}(1-0)$ line (Jackson et al. 1993; Tacconi et al. 1994) and was analyzed by Helfer & Blitz (1995) in ^{12}CO (1–0).

4.2. The nuclear kinematics from the CO position-velocity diagrams

In the inner 500 pc, the ^{12}CO (2–1) velocity field is perturbed by the two bright knots $\sim 1''$ east and west of the nucleus that do not follow the overall circular rotation. To more easily separate symmetric and asymmetric components and see which bits of the molecular gas have ordered motions, we used position-velocity diagrams (*pv* diagrams) along different angles. We made *pv* diagrams every 20° starting at 10° (**Fig. 4**). The diagram along p.a. 110° is remarkably symmetric and has most of the flux, because it crosses both emission knots. All diagrams close to the kinematic *minor* axis are compact, because there is only weak emission north and south of the center.

In ^{12}CO (2–1), the western knot (knot W) is slightly farther from the nucleus ($\sim 1.5''$) than the eastern knot. Knot W appears in *pv* diagrams at p.a. 50° and 70° , with a velocity dispersion of 60 km s^{-1} . Knot E, with a velocity dispersion of 70 km s^{-1} , appears in *pv* diagrams at p.a. 150° , 170° , 0° , and 10° as a distinct component from -230 to -30 km s^{-1} at $\sim 1.5''$ southeast of the center. To estimate these components' flux, we calculated the moments only for velocities -230 to -30 km s^{-1} . The apparent dispersion of knot W is a mixture of the 40 km s^{-1} velocity spread of the nuclear disk with the 30 km s^{-1} spread of the knot itself. For the eastern knot, it is hard to see the knot component, since it is blended with the larger-scale rotating disk. These two knots (**Table 2**) contain a few 10^6 M_\odot of molecular gas, which suggests they are giant molecular cloud complexes. There is a similar mixture in the circumnuclear molecular gas in NGC 3227, where we also found several components deviating from the overall circular rotation (SET99b).

4.3. Hints of a nuclear enclosed mass

All position-velocity diagrams show significant high velocity emission at $r \leq 0.2''$, similar to that in the nucleus of NGC 3227 (SET99b). If the high velocities trace rotation in the immediate vicinity of the nucleus, we can estimate the enclosed nuclear mass. The minimum radius at which we detect an emission peak of high-velocity nuclear molecular gas is 13.5 pc, and its mean velocity relative to systemic is $\Delta v \approx 188 \text{ km s}^{-1}$, uncorrected for inclination. If this is rotation, it implies a mass $\geq 1.5 \times 10^8 M_\odot$ within the inner 27 pc diameter, comparable with the mass of $4.5 \times 10^8 M_\odot$ within the inner 70 pc of our Galaxy (Genzel et al. 1994). This is ten times the black hole mass of $1.5 \times 10^7 M_\odot$ estimated from H₂O masers in the inner 2 pc of NGC 1068 (Greenhill & Gwinn 1997). The mass in the inner 27 pc is thus mostly due to a central, compact part of the 0.6'' (43 pc) stellar cluster as mapped by Thatte et al. (1997).

4.4. The rotation curve

The molecular gas velocity field inside the spiral arms is complex, making it hard to derive the rotation curve from ¹²CO alone. We now discuss our best estimate of the CO rotation curve and compare our results with the stellar motions. We show that the velocity fields of gas and stars are similar, reflecting the influence of the bar on the motions at $3'' < r < 15''$. We think the difference in the rotation curves of the gas and stars could be due to the complex dynamics induced by the stellar bulge.

4.4.1. Rotation curve from gas motions

The ¹²CO velocity field in the center of NGC 1068 deviates strongly from circular rotation at $r < 13''$, so a rotation curve derived from a rotating disk model would probably be wrong. The velocity field and *pv* diagrams show however, that most of the ¹²CO emission is indeed from a centro-symmetric structure. We therefore used the first-moment velocity maps of the ¹²CO (1–0) and ¹²CO (2–1) emission to determine the velocity extrema in circular annuli around the center. We chose the ¹²CO (2–1) velocity map because the high-velocity-dispersion knots on either side of the nucleus are partly resolved (**Figs. 1 and 4**). The mean velocities in these maps are lower limits to the true rotation speeds since we did not correct for inclination. Our mean curve, corrected for an inclination $i = 40^\circ$, agrees well with published rotation curves within the uncertainties (**Fig. 5**). We compared our rotation curve with that derived from H α (Dehnen et al. 1997; errors 10 to 30 km s^{-1} for $r < 16''$) and with the curve derived from the BIMA ¹²CO (1–0) data (Helfer & Blitz 1995; errors 30 to 70 km s^{-1} for $r < 16''$ and 10 to 20 km s^{-1} for $16'' \leq r < 30''$).

From $r = 2.3''$ moving inward, our ¹²CO (2–1) rotation curve first increases by 50 km s^{-1} and then decreases again at $r = 1''$. This range of radii contains the nuclear ring and the

two barely-resolved CO knots east and west of the nucleus. The pv diagrams along p.a. 110° are similar in ^{12}CO (1–0) and ^{12}CO (2–1). We derived the rotation curve at $r < 1''$ for two cases: (1) rotation velocities go to 0 km s^{-1} at the center, and (2) Keplerian velocities around a point mass interior to $r = 0.4''$ (section 4.3).

4.4.2. The stellar velocity field

Garcia-Lorenzo et al. (1997) mapped the stellar velocities in the inner $24'' \times 20''$ with the optical Ca II triplet at λ 8498, 8575, and 8695Å. The velocity field of the stars matches that of the ^{12}CO (1–0) emission to within 50 km s^{-1} and $1''$. This indicates that at $r > 3''$ (the resolution of the Garcia-Lorenzo et al. data), the stars and gas have similar kinematics. The velocity dispersion observed in the Ca II lines agrees well with the velocity dispersion derived in the NIR (Dressler 1984; Terlevich et al. 1990; Oliva et al. 1995), suggesting that the velocity field measured in the Ca II line is indeed representative of the overall nuclear region (inner $15''$ to $20''$) and does not merely trace the surface of an otherwise obscured stellar system.

For both stars and gas, at radii $\leq 10''$, the isovelocity lines in the north bend to the east, and the isovelocity lines in the south bend to the west. Such a bending is as expected from our model calculations (section 7.2) for orbits induced by a bar. It also agrees with the expected behavior of gas and stars in the potential of the NIR bar (e.g., Athanassoula 1992; Maciejewski & Sparke 1999). To confirm this finding observationally, more data are needed on the Ca II velocity field south ($\sim 8''$) of the nucleus, since the bending in the isovelocity lines occurs at a higher velocity relative to systemic than in the north. Higher-sensitivity molecular line data south of the nucleus would also be useful.

4.4.3. Rotation curve in the inner $6''$

In the inner region the kinematics of stars and gas may be decoupled. The stellar kinematic data (Garcia-Lorenzo et al. 1997) indicate that the stellar rotation curve lies well below the rotation curve derived from the ^{12}CO data. This probably reflects the fact that in the inner $6''$ the velocity dispersion of the stars is higher relative to that of the molecular gas. In this region, the gravitational force of the gas is negligible relative to that of the stars, so we estimate the effects of different stellar potentials as follows. (1) We start with the simplest model, an isotropic, spherical stellar cluster. (2) We then generalize our model to central oblate stellar systems. (3) Finally, we consider the effect of a stellar bar on stellar orbits in the center of NGC 1068.

Isotropic, spherical stellar cluster: The mass of an isotropic, spherical, non-rotating stellar cluster can be estimated from the stellar velocity dispersion and the Jeans equation, derived from the collisionless Boltzmann equation (see Binney & Tremaine 1987). Thatte

et al. (1997) assumed a velocity dispersion of 140 km s^{-1} (Dressler 1984) to estimate a mass of $6.5 \times 10^8 \text{ M}_\odot$ within the inner $2''$ diameter. This is nearly twice our value of $3.7 \times 10^8 \text{ M}_\odot$ for the same region derived from the molecular gas. The discrepancy could be due to (1) the stellar flux coming from supergiants with deeper Ca II absorption than in the template giant stars, yielding a lower apparent velocity dispersion, or (2) the velocity dispersion of the underlying bulge component, which emits up to 45% of the light in the inner $5''$ (Table 1 of Thatte et al. 1997). Comparison of I -band data in the inner $15''$, which show constant velocity dispersion (Dressler 1984), with the nuclear H and K band data indicates that the velocity spread of the nuclear cluster cannot exceed that of the outer zone. All this suggests the mass derived by Thatte et al. (1997) is an upper limit to the enclosed nuclear mass.

Central oblate system: Observations and theory suggest bars turn into bulges at small radii (Norman et al. 1996; Hasan et al. 1993; Combes et al. 1990). For these systems the Jeans equation separates into two equations giving the vertical and radial form of the gravitational potential (see review by Merritt 1999). Binney & Tremaine (1987, their Fig. 4-5) show that if self-similar isodensity ellipsoids of stellar spheroidal systems become more spherical at smaller radii then v/σ falls below unity. This is indeed indicated by K -band images for $r \leq 5''$ (e.g., Fig. 1 in Thatte et al. 1997). Hence if the observed stellar velocity dispersion is constant, the circular velocity must decrease at smaller radii. This is consistent with the observed drop in the stellar rotation curve toward the center of NGC 1068.

Influence of a bar potential: NGC 1068 has a stellar bar in the inner $20''$ seen in the NIR (Scoville et al. 1988; Thronson et al. 1989). Bars have prolate symmetry and are probably triaxial. Such a system can have an anisotropic velocity dispersion and its ellipsoid need not be coaxial with the bar (Fillmore 1986). It is thus not easy to predict the velocity dispersion, since in a bar potential, many orbit families are extended in the z -direction and there can be radial and vertical resonances that support specific orbit families, affecting the stellar velocity dispersion (e.g. Pfenniger 1984; Combes et al. 1990; Olle & Pfenniger 1998). Unlike the stars in the center of NGC 1068, the molecular gas has a low velocity dispersion (section 4.1), indicating it is decoupled from the stars. This explains why the gas rotation curve — which we used for our models — lies above the stellar rotation curve by Garcia-Lorenzo et al. (1997) at small radii. Hence, for circular orbits, the molecular gas is a good tracer of the potential and its rotation curve is governed by the enclosed dynamical mass.

4.5. The bars and resonances

The interaction of the molecular gas with the stellar gravitational potential leads to resonances that in turn determine the distribution and kinematics of the gas. We now discuss the evidence for bars and the locations of dynamical resonances in NGC 1068.

4.5.1. The Bars

Although NGC 1068 is not normally considered a barred spiral, Scoville et al. (1988) nevertheless detected at K band a $32''$ long bar at p.a. $\sim 48^\circ$. The ends of the NIR stellar bar join the spiral arms in the molecular gas (e.g., Tacconi et al. 1997). In most bar theories, there are no massive pile-ups of gas at the corotation radius near the ends of the bar. These accumulations are only expected at the inner and outer Lindblad resonances. The fact that the arms are at the bar corotation radius is thus puzzling and could indicate the dynamical effect of a second, larger bar in NGC 1068. (Here, we assume that the corotation lies about at the end of the bar as found for late type galaxies, see Combes 1997 for a review.)

Optical images of NGC 1068 show a bright inner disk at radii $< 100''$, with spiral arms and dust lanes extended north-south (see sketch in Fig. 6). This oval structure is $180''$ (~ 13 kpc) long, at p.a. 5° , with an eccentricity of 0.8 (Bland-Hawthorn et al. 1997, from *BRI* images by R.B. Tully). At radii $> 15''$, however, the *kinematic* major axis runs almost exactly east-west. Hence the eccentricity of the oval structure on the sky is not due to the galaxy's inclination; instead, this structure is *a large-scale bar along the minor axis of NGC 1068*. In the Palomar Sky Survey images of NGC 1068, the outer, weak emission (radii $> 100''$) is extended east-west, and the eccentricity of its lowest contours corresponds to the 40° inclination derived from HI velocities (Brinks et al. 1997). Deprojection of the optical image then yields a bar length of $240''$ (17.3 kpc). As shown in section 4.5.2, this bar has its inner Lindblad resonance (ILR) at $r = 18''$ (1.3 kpc), near the molecular spiral arms. The outer bar-like structure in NGC 1068 could thus be the cause of these spiral arms. Further support for this idea comes from the deprojected shape of the molecular spiral arms, which is an almost perfect ring — as expected for an ILR. It suggests the NIR bar is a second bar inside the ILR, similar to nuclear bars in other galaxies (e.g. Friedli et al. 1996).

4.5.2. Location of the Resonances

We estimated the radii of the dynamical resonances of the inner and outer bars from the rotation curve and bar lengths, using the curves of Ω and $\Omega \pm \kappa/2$, to see if they matched the sites of the gas (Fig. 7). (We follow the usual nomenclature, with Ω = angular velocity, and κ = epicyclic frequency, where $\kappa^2 = r \times (d\Omega/dr)^2 + 4\Omega^2 = 2\Omega \times (\Omega + (dv/dr))$ — see, e.g. the review by Sellwood & Wilkinson 1993).

We approximated dv/dr with the gradient $\Delta v/\Delta r$, which means the derived curves of κ and $(\Omega \pm \kappa/2)$ can have errors due to the undersampling of the rotation curve. The mean error in the angular velocity at radii $> 5''$ is $\pm 12 \text{ km s}^{-1}/\text{kpc}$ and larger for radii $< 5''$, where the velocity field is more complicated. The local maximum in the $(\Omega - \kappa/2)$ curve at $r \sim 17''$ corresponds to the maximum in the rotation curve. The change in the velocity gradient at this point results in a change in κ , which yields the maximum in $(\Omega - \kappa/2)$.

The change at this radius also occurs in the angular velocity curves of Helfer & Blitz (1995; their Fig. 18) and the stellar curves from Telesco & Decher (1988; their Fig. 6).

The outer or primary bar has a deprojected radius of $120''$ (8.7 kpc). At this radius, the HI rotation velocity is 165 km s^{-1} (Brinks et al. 1997), so the pattern speed of the primary bar is $\Omega_{P_p} \sim 20 \text{ km s}^{-1}/\text{kpc}$ with an uncertainty of $\pm 10 \text{ km s}^{-1}/\text{kpc}$ because the end of the bar does not exactly coincide with the corotation radius. As shown in **Fig. 7**, this pattern velocity Ω_{P_p} yields an outer ILR (oILR) at a deprojected radius of 1.6 kpc ($17''$ on the sky) and an inner ILR (iILR) at 1.0 kpc ($11''$ on the sky). This is identical with the location of the gas spiral arms at a deprojected distance of 1.3 kpc ($\sim 14''$ on the sky). It is thus likely that the gas spiral arms are caused by the outer bar driving molecular gas into the resonance zone, where the gas becomes trapped.

If an inner bar exists, it should have its corotation radius at the ILR of the outer bar. This means the inner, NIR bar should have a deprojected radius of ~ 1.4 kpc, as observed. This radius yields an inner-bar pattern speed of $\Omega_{P_s} \sim 140 \text{ km s}^{-1}/\text{kpc}$, which allows an ILR of the inner bar at $r < 6''$ — in the zone where we observe the nuclear gas ring. At these small radii, however, we know the rotation curve and $(\Omega - \kappa/2)$ only poorly. In contrast to our ideas, Helfer & Blitz (1995) estimated a deprojected NIR bar length of only $15''$ and thus derived an pattern speed of 160 km s^{-1} . In their interpretation, the molecular spiral arms lie between the outer Lindblad resonance and the corotation radius.

5. MOLECULAR GAS MASS AND DYNAMICAL MASS

We now discuss the molecular gas and dynamical masses for some components of the ^{12}CO line emission. These values are used to estimate the thickness of the gas disk (see section 6) and the torques acting on the disk, should it be warped (see section 7 and Appendix C in SET99b). Comparison of the molecular gas mass with the dynamical mass of the nuclear region shows that the molecular gas is a probe of the nuclear gravitational potential in NGC 1068, but not a dominant component of that potential.

Since the interferometer maps may have missed up to one half the total line emission, we derived masses only for the compact components (section 4.2). The measured fluxes $S_{\text{CO}}\Delta V$ [Jy km s^{-1}] were converted into beam-diluted, integrated brightness temperatures, in K km s^{-1} , and then multiplied by the Milky Way $\frac{N_{\text{H}_2}}{I_{\text{CO}}}$ conversion factor of 2×10^{20} $\frac{\text{cm}^{-2}}{\text{K km s}^{-1}}$ from Strong et al. (1989) to estimate H_2 column densities. We then multiplied by the beam-broadened source areas, in cm^2 , to obtain H_2 masses (**Table 2**). The calibration errors are only 15% (in the ^{12}CO (1–0) line), so the main uncertainty in the masses comes from the $\frac{N_{\text{H}_2}}{I_{\text{CO}}}$ -conversion factor, which may be wrong by at least 50% in the compact components, and even more in the extended components. In these mass estimates, since the integrated $\frac{\text{CO}(2-1)}{\text{CO}(1-0)}$ line ratio is close to unity, we assumed the two CO lines were equivalent, provided maps were convolved to the same resolution and intensities were converted to

K km s^{-1} .

We estimate the *dynamical mass*, in M_{\odot} , from $M_{\text{dyn}} = 232 v^2(r) r$, where $v(r)$ is the inclination-corrected rotation curve, in km s^{-1} , and r is in pc. The uncertainties in this mass correspond to the uncertainties in the rotation curve (section 4.4). Our value for the mass within $r = 2''$ (for circular orbits) agrees with the upper limit from Thatte et al. (1997). Most of the gas in the inner 50'' of NGC 1068 is in the molecular spiral arms, and its mass is comparable with that in the molecular ring of the Seyfert galaxy NGC 3227 (SET99b). The molecular gas mass is only 5% of the dynamical mass in the inner 50''. Even if one corrects for CO emission resolved out by the interferometer, the gas mass is less than 10% of the dynamical mass.

6. DISK HEIGHT FROM THE VELOCITY DISPERSION

The velocity dispersion observed in the molecular line emission (see **Fig. 3b and d**) is due to (1) superposition of gas at different locations on the line of sight with different velocities in the same beam and (2) the intrinsic turbulent velocity dispersion of single molecular clouds. It is this turbulence that supports the disk and determines its height.

6.1. The velocity dispersion

The velocity dispersion was measured in the second-order moment maps of the ^{12}CO lines. In the regions of enhanced flux density on the spiral arms the velocity dispersion rises to 20 km s^{-1} whereas the mean value in the spiral arms is $\sim 16 \text{ km s}^{-1}$. This mean value is similar to the HI velocity dispersion of 10 km s^{-1} for radii $> 3 \text{ kpc}$ (Brinks et al. 1997). A higher HI dispersion of 30 to 50 km s^{-1} is observed at smaller distances from the nucleus (Brinks et al. 1997). The discrepancy with the velocity dispersion measured in ^{12}CO may be due to the larger HI beam (8'') at radii $< 20''$, or to the HI disk being thicker than the molecular gas disk, as in the outer regions of our Galaxy (Malhotra 1994, 1995). For the bar region we also find a low dispersion of $\sim 16 \text{ km s}^{-1}$ in the molecular gas.

In the nucleus, the mean velocity dispersion measured in ^{12}CO (2–1) is 40 km s^{-1} , twice as high as in the spiral arms. This may be due to inclination or beam smearing rather than intrinsic turbulence in the gas. A better estimate of the velocity dispersion of the nuclear gas may be the 25 km s^{-1} spread in the systemic velocity component in the pv diagram at p.a. 110° . This is probably the value that sets the disk thickness. The high apparent velocity dispersions in the two nuclear emission knots are due to the superposition of at least two distinct components (section 4.2).

6.2. The disk thickness

To estimate the disk height from the velocity dispersion we must correct for beam smearing. We assume the observed dispersion σ_{obs} is the quadratic sum of the intrinsic dispersion, σ_{real} , and a contribution from the rotation curve σ_{rot} . We adopt an apparent velocity dispersion of $\sigma_{\text{obs,sp}} \sim 16 \text{ km s}^{-1}$ for the spiral arms and $\sigma_{\text{obs,nuc}} \sim 25 \text{ km s}^{-1}$ for the nuclear region (see above). At the spiral arms, the rotation curve is almost flat, so in this zone, the CO line widths are not affected by beam smearing. In the nuclear region, for $0.5'' < r < 1.0''$, the gradient in the rotation curve reaches $24 \text{ km s}^{-1}/\text{arcsec}$, which in a $0.7''$ beam contributes $\sigma_{\text{rot,nuc}} \sim 10 \text{ km s}^{-1}$. This only slightly increases the total apparent velocity dispersion $\sigma_{\text{obs,nuc}}$. After deconvolution, the intrinsic velocity dispersion in the nuclear region is $\sigma_{\text{real,nuc}} \sim 23 \text{ km s}^{-1}$.

There are several ways to relate the velocity dispersion σ and disk height h . Assuming hydrostatic equilibrium they can be written in their basic form as $h/r \sim \sigma/v_c$, with v_c being the circular velocity at a radius r . Quillen et al. (1992) and Combes & Becquaert (1997) derived relations for gas disks in the potentials of elliptical galaxies or galactic bulges. Downes & Solomon (1998) deduce a relation for disks with flat rotation curves following the Mestel (1963) approximation. Both approaches are relevant to the center of NGC 1068, where the potential changes from disk-like to bulge-like.

For the *spiral arms*, with a rotation velocity $v(18'') \sim 200 \text{ km s}^{-1}$ and a dispersion $\sigma_{\text{real,sp}} \sim 16 \text{ km s}^{-1}$, the equation 3.1 of Quillen et al. (1992) yields a disk height of 100 pc. For the *nuclear region*, with $v(1'') \sim 150 \text{ km s}^{-1}$ and $\sigma_{\text{real,nuc}} \sim 23 \text{ km s}^{-1}$, we get the following estimates. With eq. (3.1) of Quillen et al. (1992) we get a gas disk thickness of 10 pc. With the (third) equation of Combes & Becquaert (1997), we find a disk height of 9 pc. The application of the Mestel approximation as given by Downes & Solomon (1998, their eq. 3) with $\sigma_{\text{real,nuc}} \sim 23 \text{ km s}^{-1}$, $v(3'') \sim 170 \text{ km s}^{-1}$ and $M(\text{H}_2) \sim 5.3 \times 10^7 \text{ M}_\odot$ yields an estimate of 7 pc. All three methods thus indicate the nuclear gas disk is thin ($d \sim 10 \text{ pc}$).

7. DYNAMICAL MODELING

As noted in section 4.1, the velocity field of the central 2.5 kpc of NGC 1068 deviates from that of a simple inclined rotating disk. An obvious deviation occurs at $r \sim 10''$, where the isovelocity contour at the systemic velocity, which should be a straight line along the kinematic minor axis, is in fact inclined by 45° to the kinematic minor axis of the outer disk. Another difference to a simple disk is the complex structure in the velocity field and pv diagrams of the inner few arcseconds. Our kinematic models can fit these structures by either planar elliptical orbits due to gas moving in bar potentials, or circular orbits tilted out of the galactic plane in a warp. We first describe the best fits in pure bar models and pure warp models, and present a combined solution as the most plausible explanation. We then relate this best-fit, mixed model to observations at other wavelengths.

7.1. Outline of our model program, 3DRings

Details of our 3DRings program are in SET99b (appendix B), so we give here only a brief summary. We assume that since gas is dissipative, it persists only on orbits that are not self-intersecting, not crossing, and not strongly cusped. Its orbits can thus be of only two basic types: (1) planar elliptic orbits and (2) tilted circular orbits. The first type are the x_1 and x_2 orbits along and perpendicular to bars in the galactic plane. The second type are orbits that can leave the galactic plane, thereby warping the gas disk.

The model divides the disk into many individual circular or elliptical orbits of molecular gas. For the modeling the inclination and position angle of the disk, and the shape of the rotation curve were held fixed. Each fit was started at large radii and then extended to the center. For each case we tried several setups that all converged to similar best solutions with mean deviations from the data of $\leq 10 \text{ km s}^{-1}$ and $0.1''$ for each velocity and radius in the pv -diagrams and 10° in the position angle of the mapped structures.

For the elliptical orbit models, we follow Telesco & Decher (1988), who explained the gas motions between the two ILRs in NGC 1068 with a smoothly varying position angle of the ellipses centered on the nucleus. In the bar models, we fitted the orbital eccentricity $\epsilon(r) = b(r)/a(r)$ (where a and b are the major and minor axes) and the position angle $PA_{\text{ellipse}}(r)$ by curves varying smoothly with radius, with the orbits constrained to be non-overlapping. The orbits lie in a plane and resemble the velocity and density patterns in the bar models of Athanassoula (1992).

For the out-of-plane circular orbits, we follow the tilted ring model outlined by Rogstad et al. (1974) with a warp simulated by concentric tilted rings. The strength of the tilt and the precession of the position angles are proportional to the acting torque. The torque can result from gas moving in a non-axisymmetric potential, or from interaction of the disk gas with the radiation pressure of a nuclear source, with the gas pressure in the ionization cone of an AGN, or with some GMCs out of the disk (see SET99b, Appendix C).

To model the warp, we followed the method of Tubbs (1980; see also Quillen et al. 1992), in which the warp has a smoothly varying tilt $\omega(r)$ of each orbit relative to the disk plane and a smoothly varying precession angle $\alpha(r)$ (Fig. 8). A torque acting on an orbit with a circular velocity $v_c(r)$ induces a precession rate $d\alpha/dt \sim \xi v_c/r$. After a time Δt one obtains $\alpha(r) = \xi\Omega\Delta t + \alpha_0$, where α_0 is a constant, $\Omega = v_c/r$, and ξ is given by the acting torque. Our models had constant $\xi\Delta t$ and uniformly distributed gas.

The model fits were adjusted to match the observed pv diagrams, the velocity moment map, and the intensity map. Comparison of the models with the data was done in maps at a resolution of $0.4''$ which is super-resolved relative to the synthesized beam. This approach allowed us — especially in pv -diagrams — to concentrate on the brightest compact features in the data with a $0.7''$ beam. For both approaches we tried two rotation curves, one interpolated to 0 km s^{-1} at $r = 0''$ and one in which the observed rotation curve in the inner few parsecs was replaced with a rotation curve of a fixed enclosed mass. The best results were for a warp model with an enclosed mass of $\sim 10^8 M_\odot$.

7.2. The pure bar approach

We showed above that two bars are clearly detected in NGC 1068 and that the spiral arms are at the ILR of the outer bar (see section 4.5). In the inner 4'' the potential is dominated by the inner 1 kpc NIR bar. To be stable, an inner bar must be weaker than an outer one (e.g., Friedli & Martinet 1993). The influence of the NIR-bar on the gas motions is thus weaker than that of the outer one (Maciejewski & Sparke 1999). Furthermore, if the inner bar controlled the gas motions, the large velocity dispersion observed at a radius of 1'' would be hard to explain, since strong streaming motions are not expected for inner bars. There is also no hint in the NIR data (Thatte et al. 1997) for an additional, strong, *third* bar that could influence the structure and kinematics of the circumnuclear molecular gas.

For our pure bar model, **Fig. 9** shows the model curves for the position angle and ellipticities of the fitted ellipses, with their errors (see section 7.1). **Figure 10** compares the model *pv* diagrams with the data, and **Fig. 11** shows the model intensity distribution and velocity field. We now discuss the different regions of the model.

Spiral arms and bar region: Our best bar model gives a good fit to the data cube in the spiral arms and in the transition to the NIR bar (**Fig. 11**). In particular, the model reproduces the shifts in the alignment of the kinematic minor axis. Inspection of the velocity field on the northern part of this axis reveals the behavior of the molecular gas at an ILR and near the inner bar. At an ILR (the spiral arm region in NGC 1068), the velocity is blueshifted relative to systemic, and becomes redshifted near the NIR bar. That is, at the 30'' diameter spiral arm region, the velocity on the minor axes in both ^{12}CO (1-0) and ^{12}CO (2-1) is blueshifted relative to systemic because of the ILR of the outer large-scale bar. This velocity change along the minor kinematic axis occurs close to the spiral arms, at the transition from the x_1 orbits (those running along the outer bar, outside the oILR) to the x_2 orbits (those normal to the outer bar, between the oILR and the iILR). This outer velocity change is due to the x_2 orbit velocities being high where the x_1 orbit velocities are low.

At radii $\leq 7''$, the velocity is redshifted because of the NIR bar. At the iILR, there is a transition from x_2 orbits of the outer bar to x_1 orbits of the inner, NIR bar at p.a. 48° (Thronson et al. 1989). This is the second, inner, velocity change along the kinematic minor axis. In NGC 1068 this second shift is seen in the ^{12}CO (1-0) and ^{13}CO (1-0) lines (see section 3 and Tacconi et al. 1997; Helfer & Blitz 1995). This scenario is well matched by the orbit crowding in our model.

The nuclear gas ring: Near the nuclear ring, the bar model fails to reproduce the observed velocity increase moving in to 1'', the subsequent abrupt drop to the systemic velocity, and the observed ridge between the two CO knots (section 4.2; **Fig. 4**). This is a problem for the pure bar model, and one may ask if it could be rescued with a third bar. Fitting of the gas motions with the bar approach suggests the presence of highly elliptical east-west orbits and therefore provides evidence for the the presence of a third bar with a major axis of 1'' length. High-resolution NIR observations, however, show no such nuclear bar in NGC 1068 (Wittkowski et al. 1998; Weinberger et al. 1999; Thatte et al. 1997). The

stellar continuum in the nucleus has neither the 1" size nor the shape expected for a third bar (see Fig.2 in Thatte et al. 1997).

7.3. The pure warp approach

Another model for non-circular motions is a warp in the gas disk. The warp model yields a solution that is fully consistent with the derived gas *rotation curve*. In particular, it can explain the high velocities between 1" and 2" in the nuclear ring, seen in the *pv* diagram at p.a. 110°. (As in the bar model, for the inner few parsecs we adopted a Keplerian rotation curve for an unresolved point mass — cf. section 7.1.)

The *precession* of the warp is given by the torque ξ , the time interval Δt , the initial precession angle α_o , and the angular velocity $\Omega(r)$ of the rotation curve. For the best model, we get $\alpha_o = 10^\circ \pm 15^\circ$ and $\xi\Delta t = (7.0 \pm 0.5) \times 10^5$ yr. In this model, it is the fit to the intensity distribution that is more sensitive to changes of $\xi\Delta t$, not the fits to the *pv* diagrams. The precession time is much longer than the rotation time at $r = 1''$. At this radius, with our preferred value of $\xi\Delta t$, the disk must make 25 rotations in order to precess by 360°.

The inclination curve $\omega(r)$, which is the *tilt of the warp*, is shown in **Fig. 12** for the best fit. The errors range from $\pm 5^\circ$ to $\pm 30^\circ$. The small errors at $r = 1''$ are due to the abrupt drop in the systemic velocity at this radius, which in turn depends strongly on the inclination of individual rings.

The spiral arms and bar region: A warp can mimic spiral patterns in the plane of the sky (Steinman-Cameron et al. 1992). What about the molecular spiral arms in the center of NGC 1068? Their kinematic axis changes direction, suggesting these arms depart from circular rotation and may also be a warp effect. We found that to fit the spiral arms, the model disk must change its inclination by 20° between $r = 20''$ to 17", then stay at this new inclination down to $r \sim 2.6''$, and then flip back to the old inclination at $r = 2.2''$. One anomaly is the kinematic minor axis, which in the observed data, crosses the zero-velocity contour twice, at the spiral arms. The warp model cannot reproduce this effect. Otherwise, the warp model fits the velocity field inside $r = 17''$ just as well as the bar model does.

For the nuclear ring, **Fig. 13** compares the observed and model *pv* diagrams, and **Fig. 14** shows the intensity map and the velocity field of the warp model. For the symmetric *pv* diagram at p.a. 110° with most of the line flux, the model deviates from the data by only $\pm 5 \text{ km s}^{-1}$. In the nuclear ring, the model can explain everything in the *pv* diagram and the spectra (**Fig. 15**): the large velocity dispersion, the associated increase in velocity at 1", the emission at the systemic velocity at $r < 1''$, the decrease of velocity toward the center, and the ridge between the two high dispersion points. On the minor kinematic axis, the fit is not as good, with deviations of $\pm 20 \text{ km s}^{-1}$. This may be due to the low line flux and its contamination by sidelobes that are not completely removed by the CLEAN algorithm.

For radii $< 2.2''$ the disk starts warping, down to $r \sim 1.5''$ (110 pc) where it becomes almost edge-on ($i' = i + \omega \sim 70^\circ$). It stays at this inclination for about 35 pc (0.5'') toward smaller radii, and then warps within $r < 10$ pc from edge-on to almost face-on. Due to resolution limits, the orbit orientations at $r < 30$ pc are not well defined. The outer warped molecular gas disk (10 pc to 100 pc) probably joins continuously the inner accretion disk (~ 1 pc), which may also be warped (Gallimore et al. 1997; Greenhill & Gwinn 1997). The warped molecular gas disk may thus be not only the link between the host galaxy and the accretion disk, but also the fuel reservoir for the AGN (see section 8).

7.4. The mixed model

The bar and warp approaches both provide good fits to the data for specific regions of NGC 1068. From the observations of the two bars and the analysis of the dynamical resonances, it is obvious that the modeling of the spiral arms with elliptic orbits representing a bar potential is plausible and physically realistic. This is not necessarily true for the nuclear region, since the potential of the inner stellar (NIR) bar is weaker relative to the outer bar, and the warp approach provides a better fit to the individual components.

We thus use a hybrid model to describe the kinematics of NGC 1068, combining the best fits from both approaches. In the warp model, the tilt of the nuclear disk goes in the opposite direction of that needed to model the spiral arms. This allows us to join, at the outer edge of the nuclear ring, the warp model for the inner zone with the bar model for the outer zone. This hybrid model fits very well the intensity and velocity distributions of all the symmetric features. **Figure 16** is a perspective view of the 3-dimensional model in the plane of the sky. In this mixed model, the spiral arms are at the ILR of the outer bar. The NIR bar is an inner bar with its x_1 orbits causing the change in the position angle inside the spiral arms. The bar model of both the ILR of the outer bar (at the spiral arms) and the transition to the inner bar fits well the observed velocity field. The nuclear ring, however, cannot be reproduced very well as an ILR of the inner bar, in the same plane. The warp approach gives a better fit to the nuclear gas ring.

8. DISCUSSION

In section 4.5 we described the 17 kpc-long outer bar and the 2.7 kpc-long, NIR inner bar. Gallimore et al. (1999) recently resolved the HI absorption in the nuclear region of NGC 1068 in both space and velocity. The strongest HI is 4'' southwest of the nucleus and absorbs continuum emission of the southern radio lobe (Fig. 4 of Gallimore et al. 1999). The HI absorption velocity varies from southeast to northwest. Gallimore et al. (1999) modeled this motion with a disk inclined at the position angle of the stellar bar, and suggested the motion may be due to gas in the potential of that bar. The velocity fields of our ^{12}CO (1-0) data and our bar model confirm this conclusion. Comparison of systemic

velocity measurements (Helfer & Blitz 1995; Brinks et al. 1997; Greenhill & Gwinn 1997; this paper) suggests the value for NGC 1068 is $\sim 1120 \text{ km s}^{-1}$ rather than the 1150 km s^{-1} derived by Brinks et al. (1997) from their HI data with a $8''$ beam. This implies that the HI absorption at 1110 and 1131 km s^{-1} , seen in projection near the nucleus in the maps of Gallimore et al. (1999), is actually physically associated with the nucleus.

Friedli & Martinet (1993) made N-body simulations of double-barred galaxies and showed the dynamics inside the outer bar's ILR can be decoupled, so that an inner bar can form. This is consistent with our bar model for the ^{12}CO data. The inner and outer bars are usually assumed to have similar ILRs (Friedli & Martinet 1993; Maciejewski & Sparke 1999). So far, however, simulations of inner-bar ILRs have not been done with high enough numerical resolution to yield the details of such a region.

For the outer bar to survive, the inner bar's potential must be much weaker, implying the inner bar has a less pronounced ILR than the outer bar (Friedli & Martinet 1993). The molecular gas ring at a radius of 75 pc from the nucleus of NGC 1068 is close to the central stellar cluster (Thatte et al. 1997). The gravity of the central mass concentration competes with that of the inner, NIR bar, further weakening the inner bar's influence on the gas in the ILR region. Near the inner bar's ILR, a vertical resonance may evolve (e.g. Combes et al. 1990). Since only non-crossing orbits can retain the gas, such a vertical resonance would warp the inner molecular disk. Once out of the disk, the gas would be further supported by the potential of the central stellar cluster, competing with that of the bar.

Advantages of the warp model for the nuclear region: In summary, the reasons favoring a warp model are: (1) The best warp model reproduces all the observed symmetric structures in the CO pv diagram along p.a. 110° . (2) The warp forms an opening for the ionization cone (**Fig. 16**). (3) The warp provides enough dust between the observer and the AGN to explain why the NIR peak is offset from the optical one (see below). (4) In the inner $3''$, the polarization vectors are aligned as expected for the edge-on geometry of the molecular gas in the warp model (see below; an edge-on geometry for the central few arcsec was also proposed by Baker & Scoville (1998) and Baker (1999) to explain their CO data).

Cause of the warp: To move gas out of the plane, a torque is needed (see appendix C in SET99b). Torques can be induced by a non-spherical galactic potential (just as the halo acts on the HI disk), by radiation pressure from a radio jet (similar to central radiation sources causing warps in accretion disks; Pringle 1996; 1997), by gas pressure in an ionization cone (Quillen & Bower 1999; SET99a,b) or by the transient gravitational force of a giant molecular cloud temporarily dislocated above the plane of the disk. Arnaboldi & Sparke (1994) calculated the torque of a slightly oblate galactic potential outside the core. We assumed a similar potential, and used their eq. (B7) to estimate the torque. Our results (**Table 3**) show the most likely causes of a warp are torques induced by gas pressure, or by dislocated GMCs. The torque induced by the gas pressure of the ionization cone, for example, could persist and maintain the warp for $\sim 10^8 \text{ yr}$. A warp caused by a GMC (e.g., the western knot), deviating from the general rotation, would only perturb the galactic potential for as long as the GMC is above or below the molecular disk.

Optical dust lanes: The dust lanes in the center of NGC 1068 are obvious in the HST image with the F550M filter (Fig. 3 of Catchpole & Boksenberg 1997). To enhance the contrast, the authors subtracted a model of the nuclear starlight from the image. Their model was azimuthally symmetric, following two power laws. The model-corrected HST image nicely shows enhanced extinction running east-west. **Figure 17** compares this corrected image with the intensity distributions from the bar and warp models. This comparison favors the warp model, which predicts absorbing material at about the right locations. In a planar bar model, the extinction in front of the nuclear region can be explained only by postulating a very thick nuclear disk, which is inconsistent with disk thicknesses estimated from the velocity dispersion of the molecular gas.

The near- and mid-IR nuclear polarization: The observed near- and mid-IR polarization vectors in the inner 3" are aligned east-west (Packham et al. 1997; Young et al. 1996). For Mie scattering in an edge-on disk, light should be polarized parallel to the disk. The reason is as follows: Bands of parallel polarization vectors are often observed in bipolar stellar outflows and can be reproduced by multiple scattering models (Bastien & Menard 1988; Fischer, Henning, & Yorke 1996). These bands are often normal to the flow and occur especially in edge-on disks with high densities and particle sizes that are large relative to the wavelength of scattered light (Fischer et al. 1996). Besides strong forward and backward scattering, the Mie process also yields highly polarized emission, with the E vectors and the maximum polarized intensity both perpendicular to the direction of forward scattering. The light is strongly concentrated in two outflow cones, with the intense, back-scattered light illuminating the disk. This scattered light is then polarized parallel to the disk, over the total illuminated area (Fischer et al. 1996; Bastien & Menard 1988). Bands with parallel polarization thus occur most clearly in edge-on disks.

From the near- and mid-IR polarization maps of NGC 1068, Young et al. (1996) and Packham et al. (1997) derive scattering cones at p.a. 30° and a “torus” size of 200 pc (3"), consistent with the orbit diameters in our warp model, for the orbits with large inclinations to the line of sight. Alternatively, the alignment of the NIR polarization vectors could be due to absorption of the central stellar continuum by elongated dust grains aligned in a magnetic field by the Davis-Greenstein effect (Greenberg 1978). If so, then the magnetic field lines should lie in the plane of the absorbing gas disk, parallel to the polarization vectors. In this scenario, however, the mid-IR polarization vectors should be orthogonal to the NIR vectors, since the scattering efficiency is low at long wavelengths (unless the grains are very large), and the mid-IR flux is dust emission rather than scattered light.

9. CONCLUSIONS

1. *Molecular gas close to the nucleus.*— Our new interferometric data allow a high-sensitivity study of the molecular gas in the inner 1 arcmin of NGC 1068 at high angular ($0.7'' \times 0.7''$) and spectral resolution (10 km s^{-1}). We made detailed maps of the 200 pc-diameter nuclear ring indicated in previous molecular-line maps (Tacconi et al.

1997). We now find indications of molecular gas emission as close as 13 pc from the nucleus with a large offset from the systemic velocity. This emission suggests a mass within the inner 25 pc of $10^8 M_\odot$. This is consistent with the black hole mass of $1.7 \times 10^7 M_\odot$ indicated by the H₂O masers (Greenhill & Gwinn 1997), plus a significant contribution from the mass of the nuclear stellar cluster (Thatte et al. 1997).

2. *Bar and warp model.*— Modeling of the molecular gas kinematics in the inner 50" suggests a hybrid model combining bar-induced motion in the spiral arms and NIR bar with a warp of the thin gas disk in the nuclear ring (inner 300 pc). Due to the warping, the molecular gas leaves the plane of the disk at a radius of about 150 pc and has an inclination of $\sim 90^\circ$ to the line of sight at about 75 pc.

3. *Extinction of the nucleus.*— The obscuration of the AGN by the warped molecular gas disk is consistent with the observations of the near- and mid-IR polarization and the observed extinction of the nucleus at optical wavelengths. It explains its identification as a Seyfert 2 galaxy with a hidden Seyfert 1 nucleus.

4. *Cause of the warp.*— The probable cause for warping of the gas disk is the gas pressure in the ionization cone. This scenario is also proposed for the geometry in M 84 (Quillen & Bower 1999). Further possibilities are the influence of the transition between the disk/bar and bulge potential, or dislocated GMCs transiently disturbing the gas disk.

5. *Small tori are not needed.*— As the results by Gallimore et al. (1997) show it is very likely that NGC 1068 has a <2 pc molecular torus. However, our findings imply that the nuclear molecular gas disks may be warped providing plenty of material to occult the nuclear regions. Therefore we do speculate that long-postulated (large-scale) molecular tori with radii of a few 10 pc to a few 100 pc are not needed in every case. The more likely explanation of the Seyfert 1/Seyfert 2 differences is that the molecular gas in the center of the host galaxy contributes significantly to the obscuration of the active nucleus and thereby influences the classification (Malkan et al. 1998). In our model, the absorbing molecular clouds need no longer be confined to the galaxy's plane, in agreement with the geometry already proposed by Cameron et al. (1993) for NGC 1068. This implies that the apparent nuclear properties are strongly influenced by the distribution of gas and dust in the center of the host galaxy.

6. *The gas spiral arms are at the ILR of a large-scale outer bar.*— Analysis of the structure of NGC 1068 shows that the 3 kpc long, NIR stellar bar is an inner bar, since the galaxy also has an outer bar-like structure about 17 kpc long. This means that the spiral arms in the molecular gas (at a radius of 1.4 kpc) are at the ILR of the outer bar, in agreement with the theory of gas dynamics in barred potentials. Comparison of the velocity fields of the molecular gas and the stars with our model velocity field of a bar shows they are remarkably similar.

IRAM is financed by INSU/CNRS (France), MPG (Germany) and IGN (Spain). We thank the staff on Plateau de Bure for doing the observing, and the staff at IRAM

Grenoble for help with the data reduction, especially R. Neri, S. Guilloteau and J. Wink. For fruitful discussions we thank R. Antonucci, A. Baker, P. Englmaier, J. Gallimore, O. Gerhard, R. Maiolino, A. Quillen, N. Scoville, L. Sparke and N. Thatte. We used the NASA/IPAC Extragalactic Database (NED) maintained by the Jet Propulsion Laboratory, California Institute of Technology, under contract with the National Aeronautics and Space Administration.

REFERENCES

Antonucci, R.R.J., & Miller, J.S. 1985, *ApJ*, 297, 621.

Arnaboldi, M., & Sparke, L.S. 1994, *AJ*, 107, 958.

Arp, H. 1966, *Atlas of Peculiar Galaxies*, California Institute of Technology

Athanassoula, E. 1992a, *MNRAS*, 259, 328.

Athanassoula, E. 1992b, *MNRAS*, 259, 345.

Baker, A.J. 1999, in *The Physics and Chemistry of the Interstellar Medium*, ed. G. Winnewisser, Aachen, Shaker Verlag, in press

Baker, A.J., & Scoville, N.Z. 1998, in *The Central Regions of the Galaxy and Galaxies*, IAU Symp. 184, ed. Y. Sofue, Dordrecht: Kluwer, 221

Bastien, P., & Ménard, F. 1988, *ApJ*, 326, 334.

Binney, J., & Tremaine, S. 1987, *Galactic Dynamics*, Princeton Univ. Press, Princeton, U.S.A.

Bland-Hawthorn, J., Gallimore, J.F., Tacconi, L., Brinks, E., Baum, S.A., Antonucci, R.R.J., & Cecil, G.N. 1997, *Ap&SS*, 248, 9.

Braine, J., & Combes, F. 1992, *A&A*, 264, 433.

Brinks, E., Skillman, E.D., Terlevich, R.J., Terlevich, E. 1997, *Ap&SS*, 248, 23.

Cameron, M., Storey, J.W.V., Rotaciuc, V., Genzel, R., Verstraete, L., Drapatz, S., Siebenmorgen, R., & Lee, T.J. 1993, *ApJ*, 419, 136.

Capetti, A., Axon, D.J., & Macchetto, F.D. 1997a, *ApJ*, 487, 560.

Capetti, A., Macchetto, F.D., Axon, D.J., Sparks, W.B., & Boksenberg, A. 1995, *ApJ*, 452, L87.

Catchpole, R.M., & Boksenberg, A. 1997, *Ap&SS*, 248, 79.

Combes, F., 1997, *Extragalactic Astronomy in the Infrared*, edt. by G.A. Mamon et al., Moriond Meeting held in Les Arcs, France, 15-22 March 1997, p. 261

Combes, F., & Becquaert, J-F. 1997, *A&A*, 326, 554.

Combes, F., Debbasch, F., Friedli, D., & Pfenniger, D. 1990, *A&A*, 233, 82.

Davies, R.I., Sugai, H., & Ward, M.J. 1998, *MNRAS*, 300, 388.

Dehnen, W., Bland-Hawthorn, J., Quirrenbach, A., & Cecil, G.N. 1997, *Ap&SS*, 248, 33.

De Vaucouleurs, G, de Vaucouleurs, A., Corwin, H., Buta, R., Paturel, G., & Fougué, P. 1991, *Third Reference Catalogue of Bright Galaxies*, Berlin: Springer-Verlag

Downes, D., & Solomon, P.M. 1998, *ApJ*, 507, 615.

Dressler, A. 1984, *ApJ*, 286, 97.

Fillmore, J.A. 1986, *AJ*, 91, 1096.

Fischer, J., Geballe, T.R., Smith, H.A., Simon, M., & Storey, J.W.V. 1987, *ApJ*, 320, 667.

Fischer, O., Henning Th., & Yorke, H.W. 1996, *A&A*, 308, 863.

Friedli, D., & Martinet, L. 1993, *A&A*, 277, 27.

Friedli, D., Wozniak, H., Rieke, M., Martinet, L., & Bratschi, P. 1996, *A&AS*, 118, 461.

Gallimore, J.F., Baum, S.A., & O'Dea, C.P. 1996a, *ApJ*, 464, 198.

Gallimore, J.F., Baum, S.A., O'Dea, C.P., & Brinks, E. 1999, *ApJ* in press, astro-ph/9905267

Gallimore, J.F., Baum, S.A., O'Dea, C.P., Brinks, E., & Pedlar, A. 1994, *ApJ*, 422, L13.

Gallimore, J.F., Baum, S.A., O'Dea, C.P., Pedlar, A. 1996b, *ApJ*, 458, 136.

Gallimore, J.F., Baum, S.A., & O'Dea, C.P. 1997, *Ap&SS*, 248, 253.

García-Lorenzo B., Mediavilla E., Arribas S., & del Burgo, C. 1997, *ApJ*, 483, L99.

Genzel, R., Hollenbach, D., & Townes, C. 1994, *Rep. Prog. Phys.*, 57, 417

Greenhill, L.J., & Gwinn, C.R. 1997, *Ap&SS*, 248, 261.

Greenberg, J.M. 1978, in *Infrared Astronomy*, ed. G. Setti, G.G. Fazio, Dordrecht, 51

Hasan, H., Pfenniger, D., & Norman, C. 1993, *ApJ*, 409, 91.

Helper, T.T., & Blitz, L. 1995, *ApJ*, 450, 90.

Jackson, J.M., Paglione, T.A.D., Ishizuki, S., & Nguyen-Q-Rieu 1993, *ApJ*, 418, L13.

Kaneko, N., Morita, K., Fukui, Y., Sugitani, K., Iwata, T., Nakai, N., Kaifu, N., & Liszt, H.S. 1992, *ApJ*, 337, 691.

Khachikian, E.Y., & Weedman, D.W. 1974, *ApJ*, 192, 581.

Lumsden, S.L., Moore, T.J.T., Smith, C., Fujiyoshi, T., Bland-Hawthorn, J., & Ward, M.J. 1999, *MNRAS*, 303, 209.

Macchetto, F., Capetti, A., Sparks, W.B., Axon, D.J., & Boksenberg, A. 1994, *ApJ*, 435, L18.

Maciejewski, W., & Sparke, L.S. 1999, in proceedings of 'Galaxy Dynamics', Rutgers Univ., in press, astro-ph9812228

Malhotra, S., 1995, *ApJ*, 448, 138.

Malhotra, S., 1994, *ApJ*, 433, 687.

Malkan, M.A., Gorjian, V., & Tam, R. 1998, *ApJS*, 117, 25.

Mestel, L. 1963, *MNRAS*, 126, 553.

Merritt, D., 1999, *PASP*, 111, 247.

Muxlow, T.W.B., Pedlar, A., Holloway, A.J., Gallimore, J.F., Antonucci, R.R.J., 1996, *MNRAS*, 278, 854.

Norman, C.A., Sellwood, J.A., Hasan H., 1996, *ApJ*, 462, 114.

Oliva, E., Origlia, L., Kotilainen, J.K., Moorwood, A.F.M., 1995, *A&A*, 301, 55.

Ollé, M., Pfenniger, D., 1998, *A&A*, 334, 829.

Packham, C., Young, S., Hough, J.H., Axon, D.J., Bailey, J.A., 1997, *MNRAS*, 288, 375.

Peterson, B., 1997, *An Introduction to Active Galactic Nuclei*, Cambridge: Cambridge Univ. Press

Pfenniger, D., 1984, *A&A*, 134, 373.

Planesas, P., Scoville, N.Z., Myers, S.T., 1991, *ApJ*, 369, 364.

Pringle, J.E., 1996, *MNRAS*, 281, 357.

Pringle, J.E., 1997, *MNRAS*, 292, 136.

Quillen, A.C. & Bower, G.A., 1999, submitted to *Ap. J.*, astro-ph/9812312

Quillen, A.C., De Zeeuw, P.T., Phinney, E.S., Phillips, T.G., 1992, *ApJ*, 391, 121.

Regan, M.W., Mulchaey, J.S., 1999, *AJ*, in press, .

Rogstad, D.H., Lockhart, I.A., Wright, M.C.H., 1974, *ApJ*, 193, 309.

Rogstad, D.H., Wright, M.C.H., Lockhart, I.A., 1976, *ApJ*, 204, 703.

Sandage, A., 1961, *Hubble Atlas of Galaxies*, Carnegie Institution of Washington

Schinnerer, E., Eckart, A., Tacconi, L.J., 1999, *ApJ*, 524, L5. (SET99a)

Schinnerer, E., Eckart, A., Tacconi, L.J., 1999, *Ap.J.* submitted (SET99b)

Scoville, N.Z., Matthews, K., Carico, D.P., Sanders, D.B., 1988, *ApJ*, 327, L61.

Sellwood, J.A., Wilkinson, A., 1993, *Rep. Prog. Phys.*, 56, 173

Shlosman, I., Frank, J., Begelman, M.C., 1989, *Nature*, 338, 45

Steinman-Cameron, T.Y., Kormedy, J., Durisen, R.H., 1992, *AJ*, 104, 1339.

Strong, A. W., et al. 1987, *Proc. 20th Intern. Cosmic Ray Conf.*, I, 125

Tacconi, L.J., Gallimore, J.F., Genzel, R., Schinnerer, E., Downes, D., 1997, *Ap&SS*, 248, 59.

Tacconi, L.J., Genzel, R., Blietz, M., Cameron, M., Harris, A.I., Madden, S., 1994, *ApJ*, 426, L77.

Telesco, C.M., Decher, R., 1988, *ApJ*, 334, 573.

Terlevich, E., Díaz, A.I., Terlevich, R., 1990, *MNRAS*, 242, 271.

Thatte, N., Quirrenbach, A., Genzel, R., Maiolino, R., & Tecza, M. 1997, *ApJ*, 490, 238.

Thronson, H.A., et al. 1989, *ApJ*, 343, 158.

Tubbs, A.D. 1980, *ApJ*, 241, 969.

Weinberger, A.J., Neugebauer, G., Matthews, K., 1999, *AJ*, in press, .

Wilson, A.S., Ulvestad, J.S., 1983, *ApJ*, 275, 8.

Wittkowski, M., Balega, Y., Beckert, T., Duschl, W.J., Hofmann, K.-H., Weigelt, G., 1998, *A&A*, 329, L45.

Young, S., Packham, C., Hough, J.H., und Efsathiou, A., 1996, MNRAS, 283, L1.

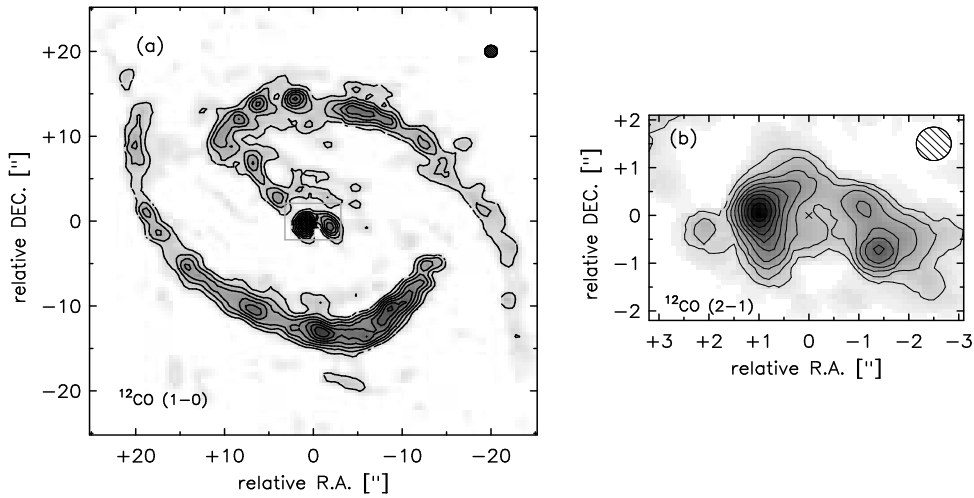


Fig. 1.— Maps of (a) ^{12}CO (1–0) and (b) ^{12}CO (2–1) in the center of NGC 1068. Contours are at 10, 20, ... 100% of the peak, which is 1.24 Jy km/s/beam in ^{12}CO (1–0) and 3.43 Jy km/s/beam in ^{12}CO (2–1). The central box in the ^{12}CO (1–0) map shows the area of the ^{12}CO (2–1) map.

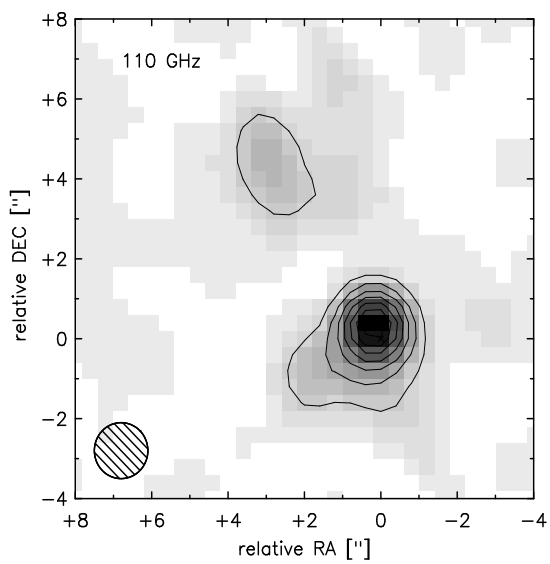


Fig. 2.— The distribution of the 110 GHz continuum in NGC 1068 with a sensitivity of $1\sigma = 1$ mJy/beam. The contours start at 3σ in steps of 3σ . The peak intensity is 23 mJy/beam.

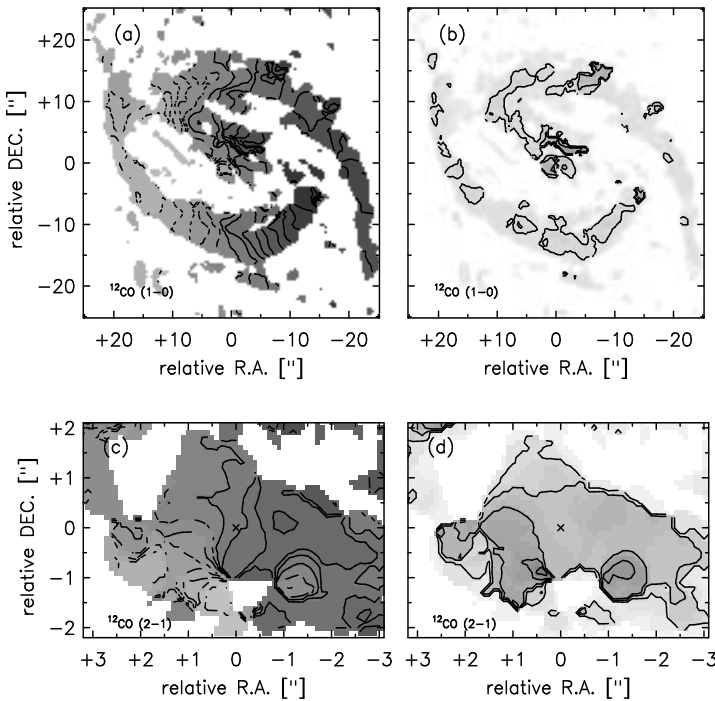


Fig. 3.— Velocity field and velocity dispersion of the ^{12}CO lines in NGC 1068. The velocity field (a) and the velocity dispersion map (b) of the ^{12}CO (1-0) emission (beam $1.4''$) and the ^{12}CO (2-1) emission (beam $0.7''$) (c and d) are shown, respectively. The contours of the velocity fields are in steps of 20 km s^{-1} ($v=0 \text{ km s}^{-1}$ corresponds to the first central solid line next to a broken line). In the dispersion maps, contours are at $15, 30, 45$ and 60 km s^{-1} for ^{12}CO (1-0) and at $15, 30, 45, 60$ and 75 km s^{-1} for the ^{12}CO (2-1).

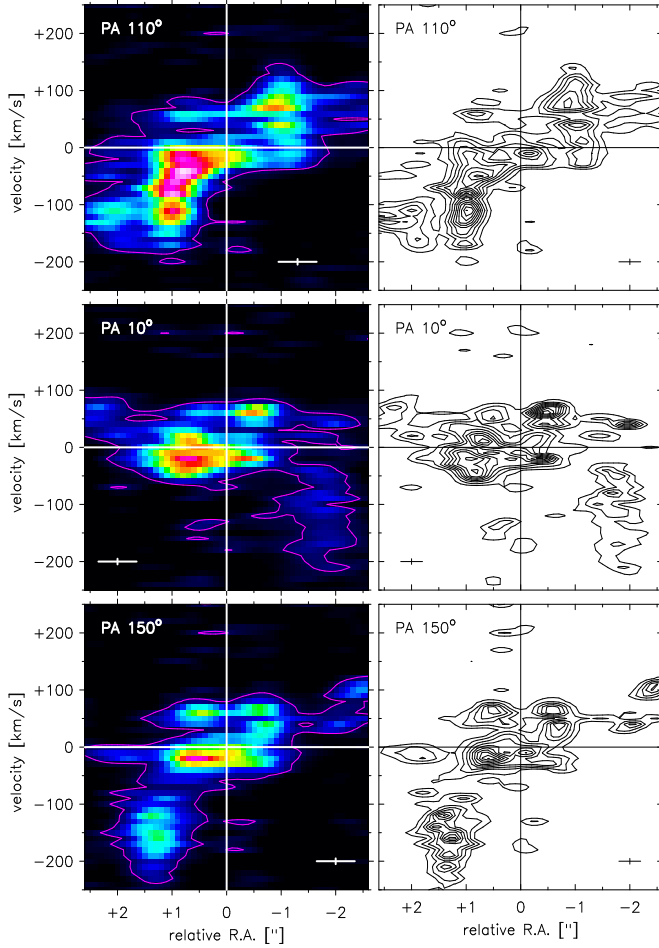


Fig. 4.— Position-velocity diagrams of the nuclear ^{12}CO (2–1) line emission in NGC 1068 along different position angles. To highlight this complex velocity behavior the data is shown at a nominal resolution of $0.4''$ (right). The contours are at 10, 30, ... 100% of the peak. For comparison the corresponding pv -diagrams at the achieved instrumental resolution of $0.7''$ are shown in color on the left panels. The velocity resolution in both cases is 10 km s^{-1} . The (magenta) contour corresponds to 3σ , with $1\sigma = 6.0 \text{ mJy/beam}$. A remarkable feature in the pv -diagram along p.a. 110° is the large velocity dispersion at $\pm 1''$ from the center. For the first time in NGC 1068, we can trace molecular gas at $\approx 0.18''$ (13 pc) from the nucleus. The high velocities in this region imply an enclosed mass of $\sim 10^8 \text{ M}_\odot$ not correcting for inclination effects. This value is consistent with a black hole mass of $1.7 \times 10^7 \text{ M}_\odot$, as estimated from nuclear H_2O maser emission (Greenhill & Gwinn 1997), plus a contribution from a compact nuclear stellar cluster (Thatte et al. 1997).

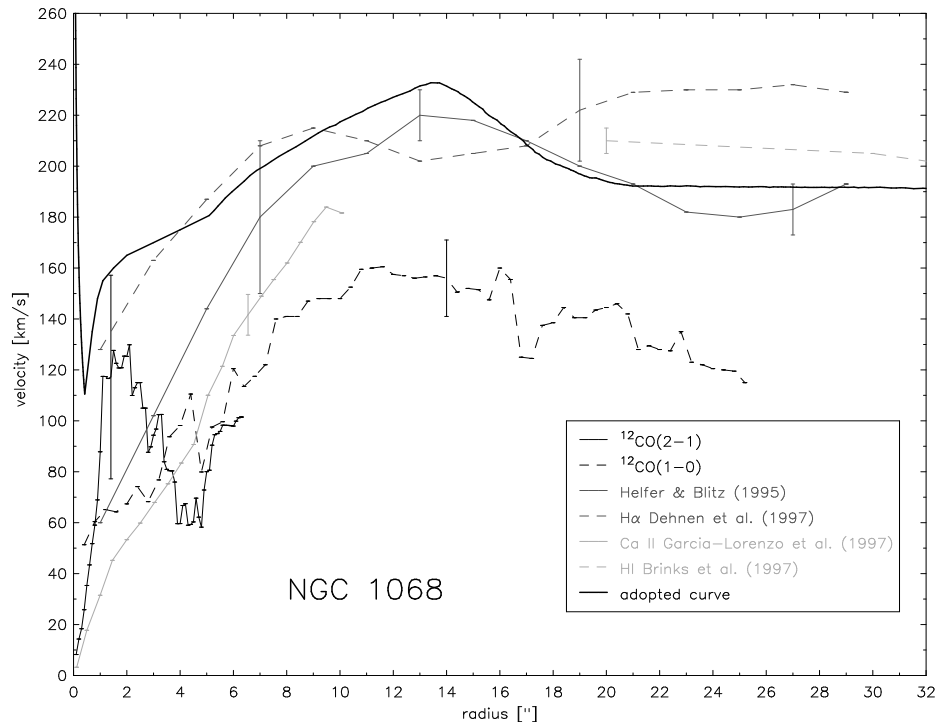


Fig. 5.— Rotation curves for NGC 1068. The ^{12}CO curves are the average values of the minimum and maximum velocity at any given radius (uncorrected for inclination). The other curves are taken from the quoted references. The increase in velocity of the ^{12}CO (2–1) curve at a radius of $r \sim 1''$ can also be seen in the pv diagrams of the observed data. At radii between $10''$ and $16''$ the rotation curve agrees with fits of a rotating gas disk to the observed data.

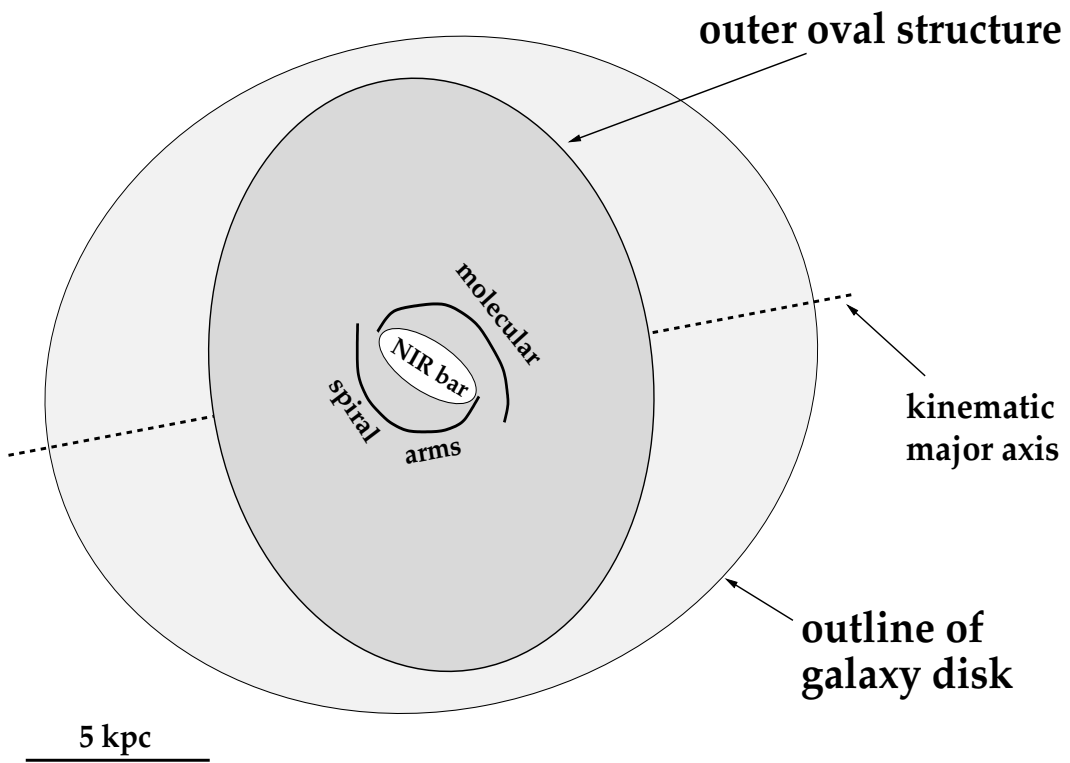


Fig. 6.— Sketch of NGC 1068 showing the location of the bars and molecular spiral arms. With the exception of the outline of the galaxy disk the figure is approximately to scale.

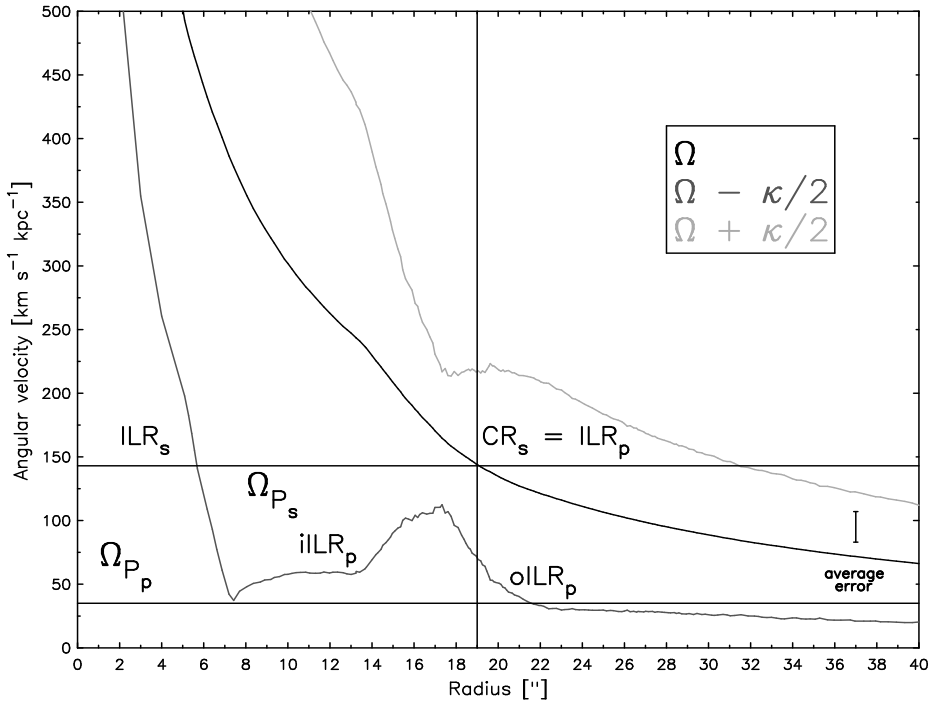


Fig. 7.— Sites of inner Lindblad resonances (ILRs) and corotation resonances (CRs) in NGC 1068. The ILR_p of the outer, primary bar is at the molecular spiral arms at $r \sim 18''$. If an inner, secondary bar exists, its CR_s coincides with the ILR_p of the outer bar. The outer, primary bar has a deprojected radius of about $120''$ translating into a CR at about $140''$. (See text.)

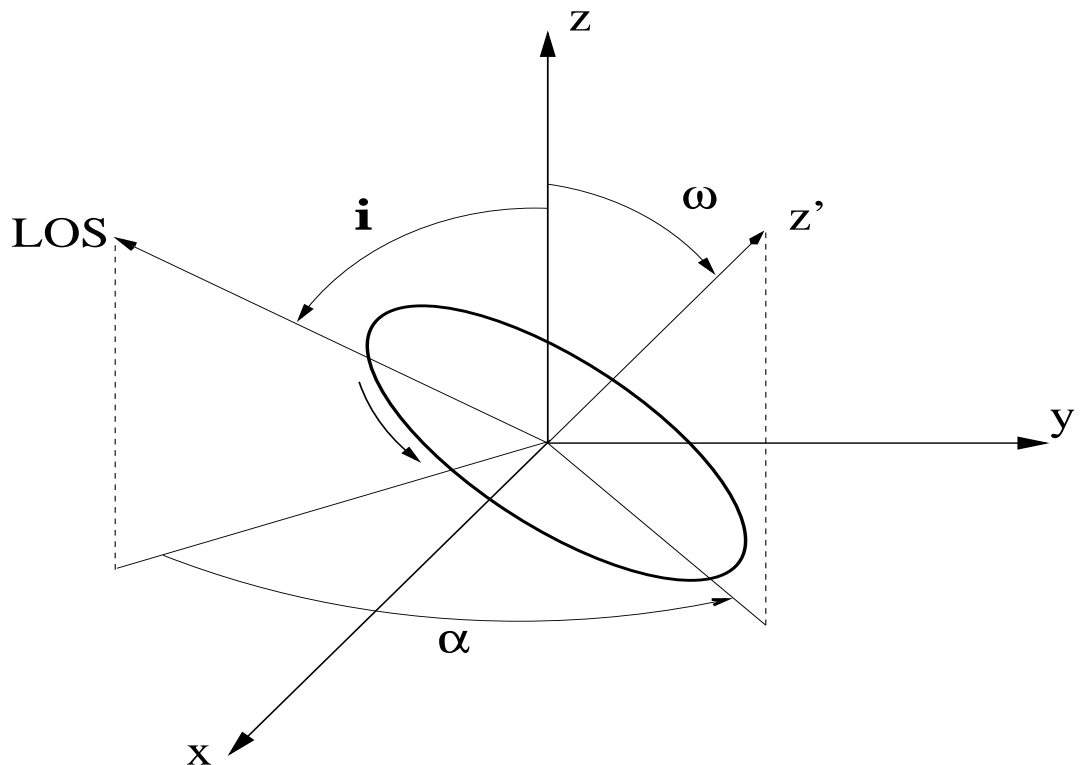


Fig. 8.— Parameters in the 3DRings warp model. The diagram shows only a single ring, tilted by an angle ω relative to the galaxy's rotation axis, which is inclined at angle i to the line of sight. Here α is the precession angle between the projection of the line of sight on the plane of the galaxy and the ring axis.

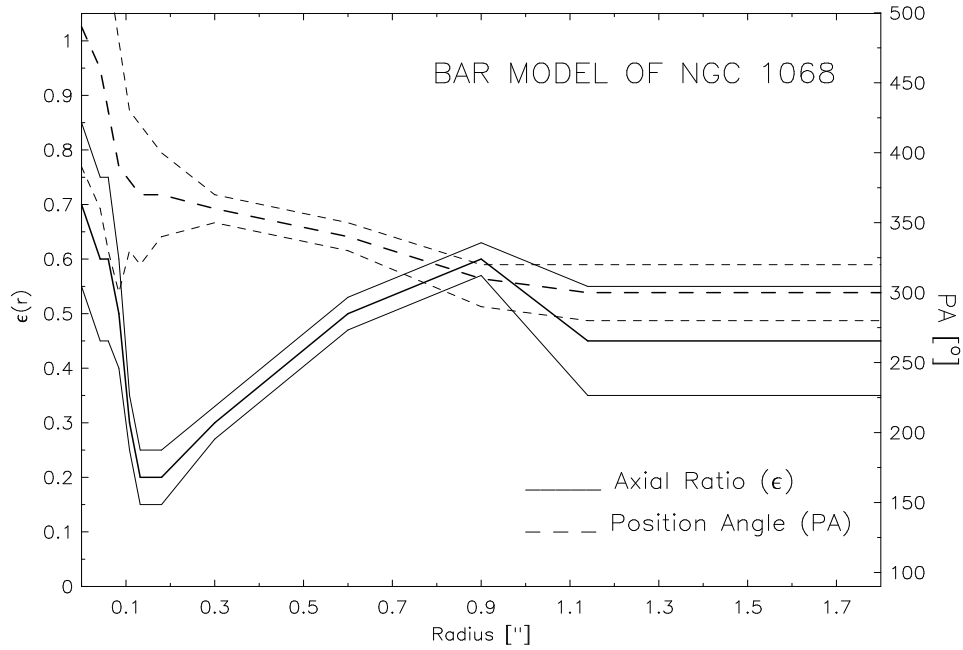


Fig. 9.— The curves of position angle PA and ellipticity ϵ of the elliptical orbits in the bar model that fit the data. The curves of ϵ (solid line) and PA (broken line) are shown as thick lines for the best fit, and as thin lines over the range of satisfactory fits (see text).

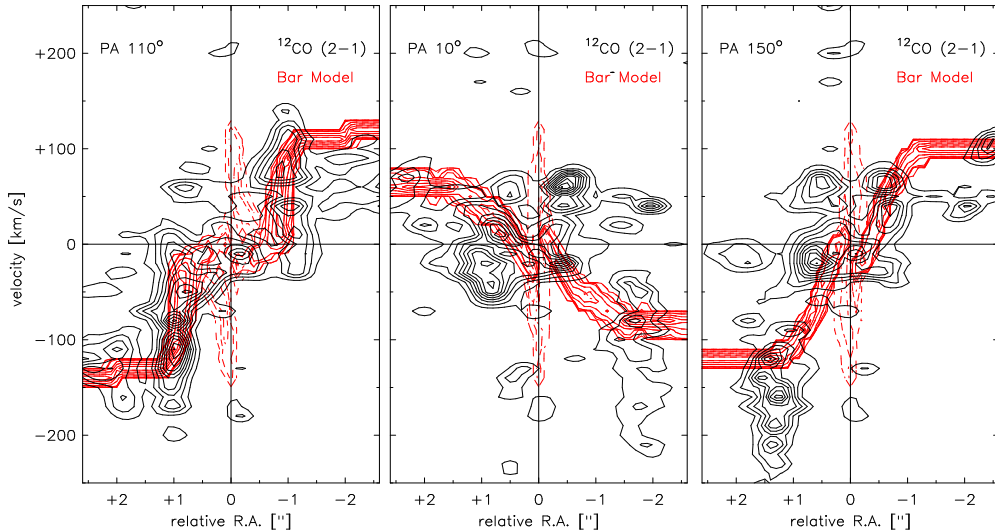


Fig. 10.— Position-velocity diagrams for the bar model in NGC 1068. The regions of high velocity dispersion that appear at low intensity (p.a. 10° , radius $-1.8''$ and p.a. 150° , $r = 1.3''$) are molecular cloud complexes that are not part of a symmetric velocity field (see section 4.2). The bar model explains all symmetric velocity structures. Although the bar model can fit the component at lowest velocities, it cannot explain the high velocity dispersion of these components. The data at $0.4''$ resolution are shown in black contours of 10 to 100% in steps of 10%. The model, calculated for a starting radius of 27 pc, is shown in red contours at 0.2, 2, 5, 20, 40, 60 and 80 %.

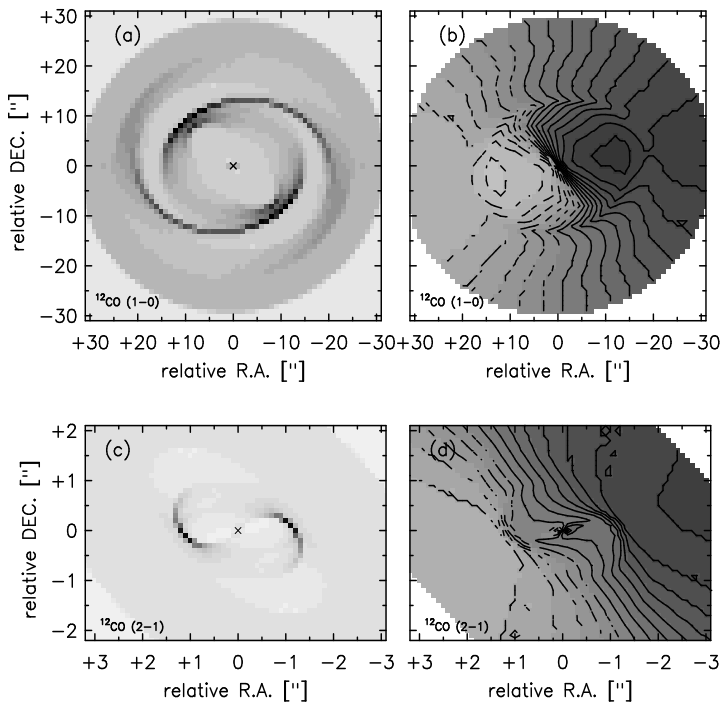


Fig. 11.— Intensity maps (*left*) and velocity fields (*right*) of the bar model for the ^{12}CO emission (*a and b*: ^{12}CO (1–0) , *c and d*: ^{12}CO (2–1)). Velocity contours are from -150 to 150 km s^{-1} in steps of 20 km s^{-1} for ^{12}CO (1–0) and from -130 to 130 km s^{-1} in steps of 20 km s^{-1} for ^{12}CO (2–1) . Broken lines indicate negative velocities.

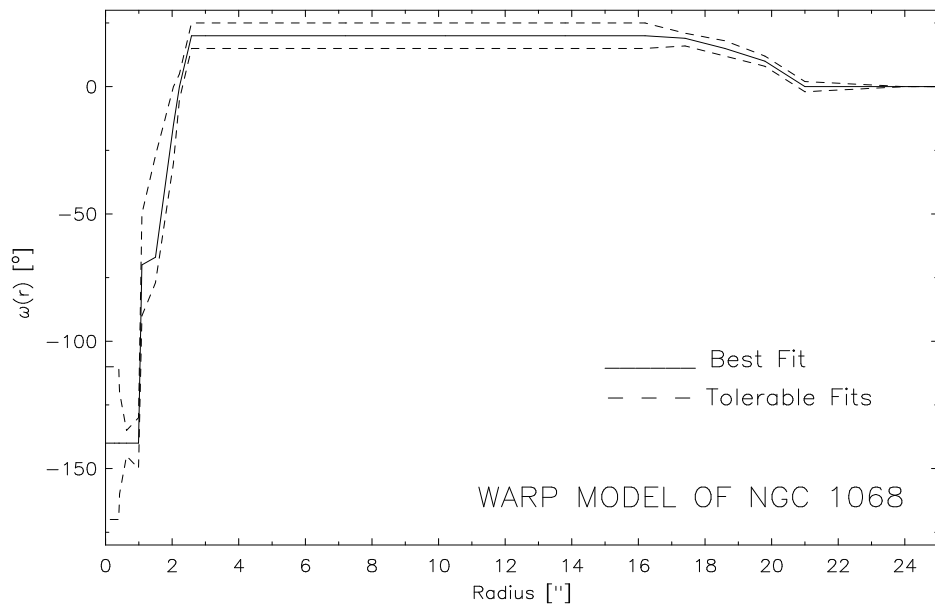


Fig. 12.— The ω (angular velocity) curve of the warp model. The solid line shows the best fit to the data. Broken lines indicate the range over which the fits are satisfactory.

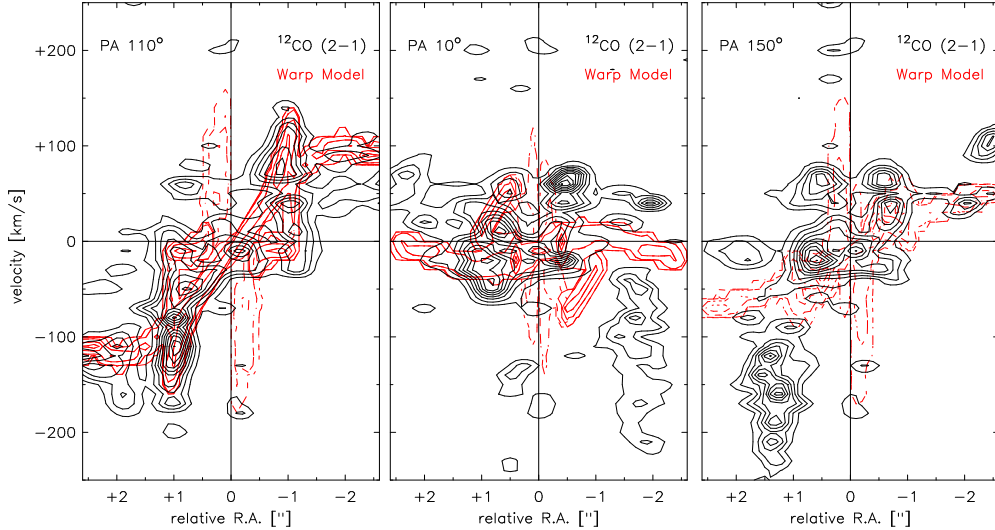


Fig. 13.— Position-velocity diagrams for the warp model in NGC 1068. The weak emission regions of high velocity dispersion (at p.a. 10° , $r = -1.8''$ and p.a. 150° , $r = 1.3''$) belong to molecular cloud complexes which are not part of a symmetric velocity field (see section 4.2). Our model only explains symmetric structures. The contrast-enhanced data are in black contours of 10 to 100% in steps of 10%. The model, calculated starting from $r = 27$ pc, is shown in red contours at 0.2, 3, 20, 50 and 80 %.

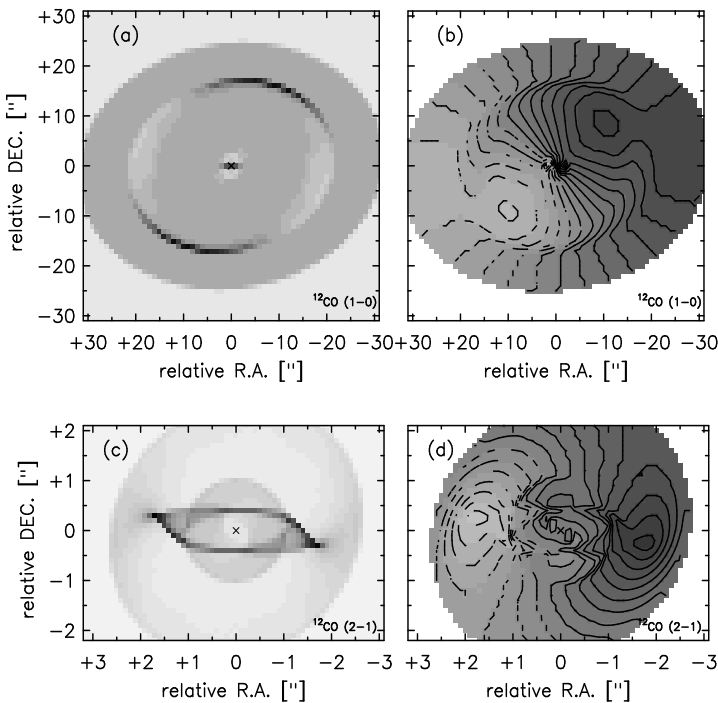


Fig. 14.— Intensity maps (*left*) and velocity fields (*right*) of the warp model for the ^{12}CO emission (*top*: ^{12}CO (1-0) , *bottom*: ^{12}CO (2-1)). Velocity contours are from -150 to 150 km s^{-1} in steps of 20 km s^{-1} for ^{12}CO (1-0) and from -130 to 130 km s^{-1} in steps of 20 km s^{-1} for ^{12}CO (2-1) . Broken lines indicate negative velocities.

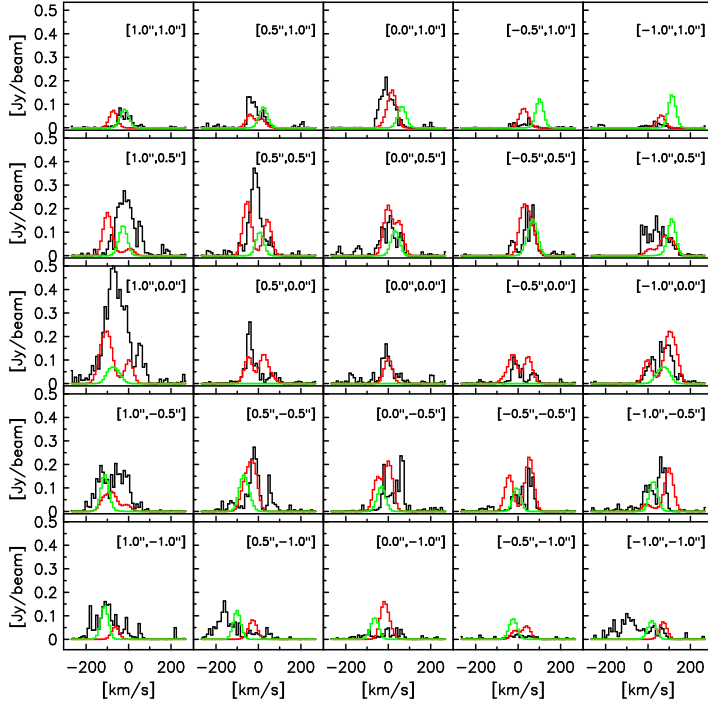


Fig. 15.— Comparison of measured spectra (*black*) with those given by the warp model (*red*) and the bar model (*green*), in the central $2'' \times 2''$ in steps of $0.5''$. Intensity scales are arbitrary. With the exception of the eastern knot (knot E) the warp model represents an acceptable fit to the observed data that reflect the complex velocity field. The agreement of the bar model with the data is not as good as it cannot reproduce the multiplicity (two features) of the line, especially at positions west and south-west of the nucleus.

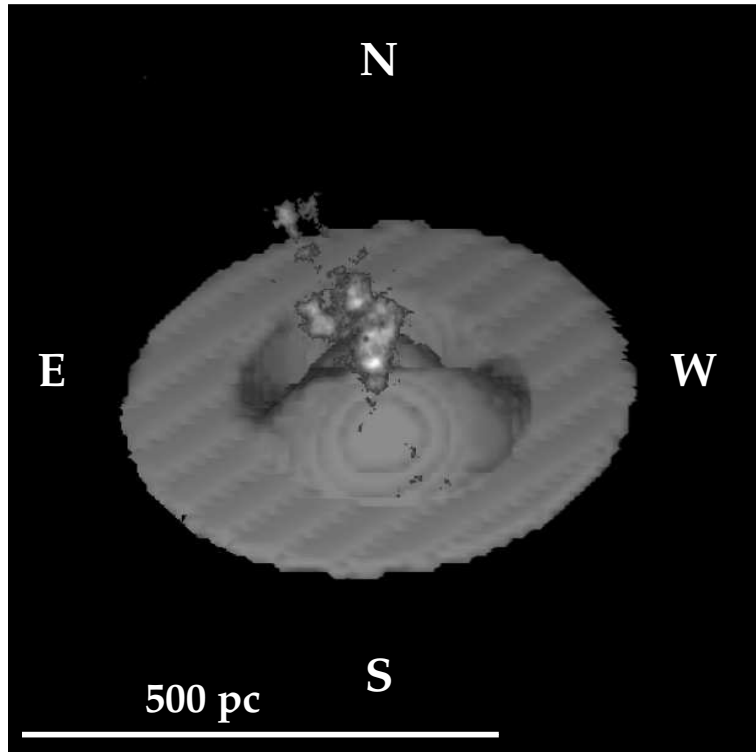


Fig. 16.— Geometry of the NGC 1068 warp model. Brighter sections are closer to the observer, darker ones are farther away. The brightest structure is the [O III] ionization cone (Macchetto et al. 1994). The 3-dimensional geometry of the warp creates a natural cavity for the ionization cone that is consistent with its observed orientation.

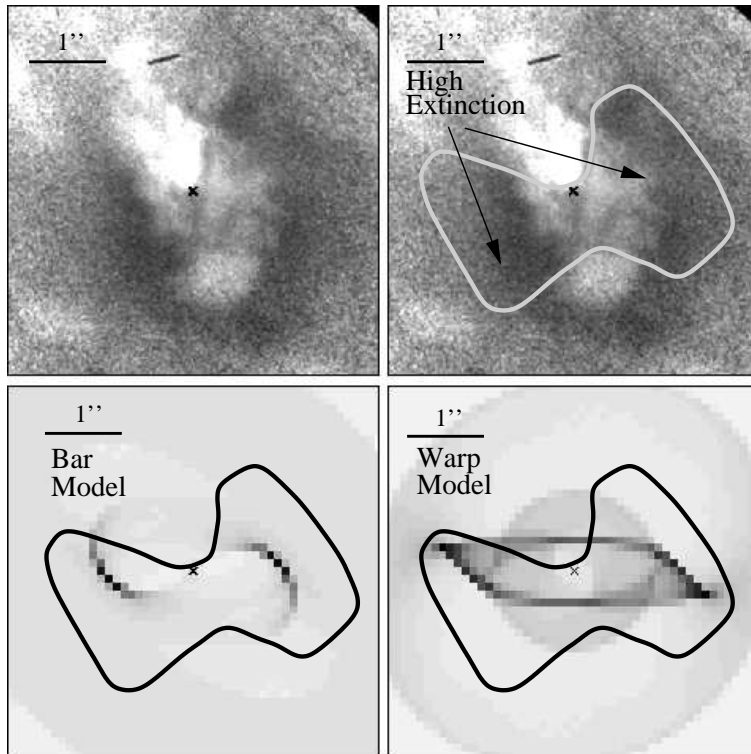


Fig. 17.— The F550M filter HST image (*top left*) of the central $4'' \times 4''$ in NGC 1068 divided by a model of the stellar light (see text and Catchpole & Boksenberg 1997). The dust lane is encircled by the solid gray line in (*top right*). The *bottom right* image shows that the CO intensity predicted by the warp model agrees with the dust distribution. The agreement is not as good for the bar model (*bottom left*), which does not predict the gas and dust concentration above and below the nucleus.

Table 1: Properties of NGC 1068

NGC 1068	
Right ascension (J2000)	02 ^h 42 ^m 40.798 ^s
Declination (J2000)	−00° 00' 47.938"
Classification	(R)SA(rs)b
Inclination	40°
Position angle	278°
AGN Type	Sey 2
Systemic velocity	1150 km s ^{−1}
Distance	14.4 Mpc

Nuclear coordinates are from Muxlow et al. (1996). Systemic velocity and Seyfert type are from NED (NASA/IPAC Extragalactic Database). The host galaxy classification is from de Vaucouleurs et al. (1991). Inclination and position angle are from the “Ringberg standards” (Bland-Hawthorn et al. 1997).

Table 2: Molecular gas masses of various compact components in NGC 1068

component	S_{CO}	ΔV	$M(\text{H}_2)$	M_{dyn}
	[Jy km/s]		[$10^7 M_{\odot}$]	[$10^8 M_{\odot}$]
total		670	68	120
spiral arms		560	57	
Northern bar		2140	5	
ring in ^{12}CO (2–1)		20	5	9
knot E		12	0.3	
knot W		8	0.2	

Uncertainties in gas masses are 40% for the compact components and 50 % for the extended components. Uncertainties of dynamical masses are dominated by rotational velocity errors. The fluxes were derived for the total line width with exception of the two knots in the ring for which we used only velocities from -230 to -30 km s^{-1} . The flux of knot E was measured in a rectangle with corners at $-1.3''/ -2.0''$ and $0.6''/ -0.9''$ and knot W in a rectangle with corners at $0.8''/ -1.3''$ and $1.9''/ -0.4''$. The dynamical mass was derived with the equation in the text, with our molecular gas rotation curve at radii of $18''$ and $2''$.

Table 3: Causes for the warp in NGC 1068

Cause	Property	Value
Estimated via		
3DRings^a	torque¹	M 1.9×10^{47} Nm
	molecular gas mass	m $2.0 \times 10^6 M_{\odot}$
	radius	r 2.2×10^{18} m
	velocity	$v(r)$ 140 km s ⁻¹
	time of circulation	$\dot{\Phi}^{-1}$ 4.0×10^{13} s
potential^b	torque²	M 7.6×10^{10} Nm
	molecular gas mass	m $2.0 \times 10^6 M_{\odot}$
	volume	V_o 1.5×10^{56} m ³
	total mass	$m_o = \rho_o V_o$ 4.3×10^8
GMC^c	torque³	m 3.2×10^{44} Nm
	cloud mass	m_{GMC} $2.0 \times 10^6 M_{\odot}$
	force	F 9.5×10^{25} N
	lever arm	$l = r$ 3.3×10^{18} m

see caption of next table

^{E1}NOTE TO EDITOR: The following two tables should be one; table caption is incomplete in processed file (ps-file)

Table 4: Causes for the warp in NGC 1068 continued

gas pressure ^d	torque ⁴	M	1.6×10^{46} Nm
particle density	$\frac{N}{V}$		10^4 cm ⁻³
temperature	T		1.0×10^5 K
gas pressure	p		1.4×10^{-8} N m ⁻²
area	A		5.5×10^{35} m ²
lever arm	l		2.1×10^{18} m
radiation pressure ^e	torque ⁵	m	4.8×10^{40} N m
spectral index	α		~ -1.0
constant	b		1.0×10^{-17} W m ⁻²
luminosity	L		6.6×10^{32} W
intensity	I		1.2×10^{-5} W m ⁻²
radiation pressure	p		3.9×10^{-14} N m ⁻²
area	A		5.5×10^{35} m ²
lever arm	l		2.1×10^{18} m

Physical reasons for the warp of circum-nuclear gas disks are summarized in the conclusions (section 9) and given in detail in the appendix C in SET99b. In this table first order estimates are based on:

^a from SET99b, eq. C3. ; ^b from SET99b, eq. C2. ; ^c from SET99b, eqs. C1 and C4. ; ^d from SET99b, eqs. C1 and C5. ; ^e from SET99b, eqs. C1 and C6.

¹ from the parameters of 3DRings for an inner disk, with $r = 108$ pc

² from the mass of warped nuclear gas disk and a dynamical mass within $r < 108$ pc.

³ from mass of knot W at $r = 108$ pc and its distance relative to the gas disk.

⁴ N/V and T of ionization cone from Capetti et al. (1997a) and Gallimore et al. (1996a,b) for jet components C and NE. $A = 0.5'' \times 0.25''$ at $r = 1''$, from radio jet map.

⁵ spectral index, constant b , and area ($0.5'' \times 0.25''$) of jet at $r = 72$ pc from Gallimore et al. (1996b).